

## Article

# Study of the Applicability of Magnetic Iron-Containing Nanoparticles in Hyperthermia and Determination of Their Resistance to Degradation Processes

Assel Nazarova <sup>1,2</sup>, Artem L. Kozlovskiy <sup>1,3,\*</sup> , Vyacheslav S. Rusakov <sup>4</sup> , Kamila B. Egizbek <sup>1</sup>, Maxim S. Fadeev <sup>4</sup>, Bekzat A. Prmantayeva <sup>1</sup>, Dorota Chudoba <sup>2</sup>, Maxim V. Zdorovets <sup>1</sup>  and Kayrat K. Kadyrzhanov <sup>1</sup>

<sup>1</sup> Engineering Profile Laboratory, L. N. Gumilyov Eurasian National University, Satpayev St., Nur-Sultan 010008, Kazakhstan

<sup>2</sup> Frank Laboratory of Neutron Physics, International Intergovernmental Organization Joint Institute for Nuclear Research, 141980 Dubna, Russia

<sup>3</sup> Institute of Geology and Oil and Gas Business, Satbayev University, Almaty 050032, Kazakhstan

<sup>4</sup> Faculty of Physics, M. V. Lomonosov Moscow State University, 119991 Moscow, Russia

\* Correspondence: kozlovskiy.a@inp.kz; Tel./Fax: +7-7024413368



**Citation:** Nazarova, A.; Kozlovskiy, A.L.; Rusakov, V.S.; Egizbek, K.B.; Fadeev, M.S.; Prmantayeva, B.A.; Chudoba, D.; Zdorovets, M.V.; Kadyrzhanov, K.K. Study of the Applicability of Magnetic Iron-Containing Nanoparticles in Hyperthermia and Determination of Their Resistance to Degradation Processes. *Crystals* **2022**, *12*, 1816. <https://doi.org/10.3390/cryst12121816>

Academic Editors: Yao Wang, Jincai Chen and Lei Chen

Received: 9 November 2022

Accepted: 12 December 2022

Published: 13 December 2022

**Publisher's Note:** MDPI stays neutral with regard to jurisdictional claims in published maps and institutional affiliations.



**Copyright:** © 2022 by the authors. Licensee MDPI, Basel, Switzerland. This article is an open access article distributed under the terms and conditions of the Creative Commons Attribution (CC BY) license (<https://creativecommons.org/licenses/by/4.0/>).

**Abstract:** The article presents the results of evaluating the applicability of various types of iron-containing nanoparticles in magnetic hyperthermia, as well as determining the degradation resistance of nanoparticles. The objects of study were iron-containing nanoparticles obtained by chemical precipitation and subsequent modification with gold, gadolinium, and neodymium. The main methods for studying the properties of the synthesized nanoparticles were transmission electron microscopy, X-ray phase analysis, and Mössbauer spectroscopy. Evaluation of the efficiency of the use of the synthesized nanoparticles in magnetic hyperthermia showed that Fe<sub>3</sub>O<sub>4</sub>@GdFeO<sub>3</sub> nanoparticles, for which the specific absorption rate was more than 120 W/g, have the highest efficiency. An assessment of the resistance of the synthesized nanoparticles to corrosion in water at different temperatures showed that Fe<sub>2</sub>O<sub>3</sub>@NdFeO<sub>3</sub> and Fe<sub>3</sub>O<sub>4</sub>@GdFeO<sub>3</sub> nanoparticles have the highest resistance to degradation. It has been established that in the case of the initial Fe<sub>3</sub>O<sub>4</sub> nanoparticles, the degradation processes are accompanied by partial destruction of the particles, followed by amorphization and destruction, while for Fe<sub>2</sub>O<sub>3</sub>@NdFeO<sub>3</sub> and Fe<sub>3</sub>O<sub>4</sub>@GdFeO<sub>3</sub> nanoparticles, the degradation processes proceed much more slowly, due to the presence of interfacial boundaries, which slow down the corrosion processes. The obtained results of corrosion tests in aqueous media make it possible to predict the area and time frame of applicability of iron-containing nanoparticles when using them in the biomedical direction, as well as to determine storage conditions.

**Keywords:** iron-containing nanoparticles; magnetic hyperthermia; magnetic structures; degradation rate; core-shell

## 1. Introduction

As is known, the active study of the effectiveness of the use of magnetic nanoparticles in hyperthermia has been carried out over the past few years, and interest in these studies is due to the unique properties of nanostructures, which make it possible to reduce the exposure time, while heating occurs due to losses of nanoparticles from magnetorelaxation [1–3]. Interest in this area is also due to the fact that magnetic nanoparticles are able to convert electromagnetic energy into thermal energy in a fairly local area, which can be used to destroy cancer cells or various pathogens [4,5]. As a rule, in the case of magnetic hyperthermia, heating as a result of the transformation of electromagnetic energy into thermal energy can occur due to the effects of induction from an applied alternating pulsed field, as a result of frictional heating caused by the interaction of nanoparticles with the environment, or by relaxation losses of nanoparticles when exposed to an electromagnetic

field [6,7]. In the case of magnetic nanoparticles, due to their small size, such effects are very effective and also have a pronounced dependence on the structural properties of nanoparticles and their phase composition, which varies with changing conditions for obtaining or further modifying nanostructures [8–10].

Despite large prospects for the use of nanoparticles in magnetic hyperthermia, as well as its use for the treatment of cancerous tumors or the destruction of pathogens, there are still a number of unresolved issues and a large number of gaps in this direction. One of these important issues is the selection of optimal nanostructures that are both highly resistant to external influences, including corrosion when in aggressive or aqueous media, and have high absorption capacity and heat release, which are very important indicators in magnetic hyperthermia [11–13]. In this direction, iron-containing nanoparticles modified in various ways have great prospects, which lie in the possibility of increasing the efficiency of their use in hyperthermia. For example, it was shown in [14] that the formation of nanoparticles of the  $\text{CuFe}_2\text{O}_4$  type leads to an increase in the specific absorption rate (SAR) by a factor of 1.5–2 compared to  $\text{Fe}_3\text{O}_4$  nanoparticles. Similar effects were established in [15], where it was shown that the formation of magnetic Cobalt ferrite nanoparticles with a reverse spinel structure leads to an increase in the efficiency of their use in magnetic hyperthermia. In this regard, in the last few years, much attention has been paid to works devoted to various studies related to the search for optimal types of nanoparticles, as well as the evaluation of the effectiveness of their use in magnetic hyperthermia [16–18].

The main purpose of this work is to study the effectiveness of various modifications of iron-containing nanoparticles when using them in magnetic hyperthermia. The relevance of this work consists in determining the possibilities of using the proposed methods for obtaining nanoparticles (two-stage method) to create the most effective types of nanoparticles for magnetic hyperthermia. The choice of chemical precipitation as the main method for obtaining iron oxide nanoparticles makes it possible to obtain a sufficient amount of the base material for nanoparticles, which can be modified by various modification methods (coprecipitation or mechanochemical synthesis) and impart new properties to them, making it possible to expand the range of their application in biomedicine. The use of the proposed modification methods will make it possible to scale this technology for industrial production, and the results of experiments to determine the resistance to degradation in aqueous solutions will make it possible to determine the storage and operation conditions of nanoparticles. The novelty of this study consists in the preparation of new types of magnetic nanoparticles using a combination of chemical precipitation and mechanochemical synthesis methods, as well as a comprehensive study of their physicochemical and magnetic properties and an assessment of the prospects for application in biomedicine, in particular in magnetic hyperthermia. The choice of modification options, including the creation of structures of the “core-shell” type or doped with Gd, Nd, with the possibility of obtaining structures of complex oxides, is due to a change in their structural and magnetic properties, which can have a significant effect on the stability of materials during prolonged exposure or being in aqueous solutions, as well as the efficiency of heating and heat transfer. An important part of the work is the description of the results of experimental studies related to the determination of the stability of nanoparticles when tested in aqueous solutions. These experimental works will make it possible to determine the resistance of nanoparticles to corrosion and degradation, as well as to establish their scope and time frame of applicability.

## 2. Experimental Part

### 2.1. Materials

For the synthesis of iron-containing nanoparticles, as well as their modification by chemical coprecipitation of the gold shell and mechanochemical synthesis, the following chemical reagents were used:  $\text{FeCl}_3 \times 6\text{H}_2\text{O}$ ,  $\text{Na}_2\text{SO}_3$ ,  $\text{AuCl}_3$ ,  $\text{Nd}_2\text{O}_3$ ,  $\text{Gd}(\text{NO}_3)_3 \times 6(\text{H}_2\text{O})$ . The chemical purity of these compounds was 99.95%; all reagents were purchased from Sigma Aldrich (St. Louis, MO, USA).

## 2.2. Objects of Study

Five types of nanoparticles were chosen as objects of study: (1) initial  $\text{Fe}_3\text{O}_4$  nanoparticles (S0); (2)  $\text{Fe}_3\text{O}_4$  nanoparticles annealed at 600 °C, which are characterized by the hematite (S1) phase; (3) nanoparticles representing  $\text{Fe}_3\text{O}_4$  nanoparticles coated with gold and annealed at a temperature of 600 °C (S2); (4)  $\text{Fe}_3\text{O}_4$  nanoparticles doped with  $\text{Gd}(\text{NO}_3)_3 \times 6(\text{H}_2\text{O})$  using the mechanochemical mixing method and subsequently annealed at a temperature of 600 °C for 5 h (S3); (5)  $\text{Fe}_3\text{O}_4$  nanoparticles doped with  $\text{Nd}_2\text{O}_3$  using the mechanochemical mixing method and subsequently annealed at a temperature of 600 °C (S4).

All samples for these studies were obtained at the Laboratory of Engineering Profile of the L.N. Gumilyov Eurasian National University (ENU, Astana, Kazakhstan). These samples were synthesized using the standard technique of chemical precipitation of iron-containing nanoparticles with subsequent modification of the obtained nanoparticles in various ways.

The initial nanoparticles were obtained by dissolving 3.25 g of  $\text{FeCl}_3 \times 6\text{H}_2\text{O}$  in 100 mL of water with the addition of 5 mL of  $\text{Na}_2\text{SO}_3$  (5%). The resulting mixture was mixed with 20 mL of ammonia in an argon environment and then heated at 70 °C for 30 min. After that, the resulting mixture was heated to 90 °C with the addition of citric acid for 90 min. After washing, the resulting precipitate of iron-containing nanoparticles was placed in sealed containers in order to avoid oxidation processes in air and to initiate corrosion processes.

Chemical coprecipitation for coating iron-containing nanoparticles with a gold shell, as well as the method of mechanochemical synthesis for creating iron-containing nanoparticles of neodymium and gadolinium compounds, were chosen as modification methods.

Mechanochemical mixing of samples S3 and S4 was carried out using a planetary mill PULVERISETTE 6 classic line (Fritsch, Berlin, Germany). Mixing was carried out in a glass of tungsten carbide in the ratio of grinding media and mass of the sample 3:1, grinding speed was 400 rpm, grinding time 1 h.

All samples after synthesis and subsequent modification using the method of coprecipitation or mechanochemical synthesis were annealed in a muffle furnace at a temperature of 600 °C for 5 h, followed by cooling the samples together with the furnace for 24 h. Thermal annealing was used to form structurally ordered nanoparticles in the form of two-phase composites.

The choice of an annealing temperature of 600 °C for the samples under study is due to previous studies [11] aimed at studying the processes of phase transformations in iron oxide depending on the annealing temperature. According to the studies carried out in [11], it was found that with an increase in the annealing temperature above 400 °C, a phase transformation of the  $\text{Fe}_3\text{O}_4$ —magnetite  $\rightarrow$   $\text{Fe}_2\text{O}_3$ —hematite type was observed, followed by the formation of structurally ordered particles, the average size of which had a pronounced dependence on the annealing temperature (at high temperatures, the formation of large agglomerates of particles larger than 100–150 nm was observed). At the same time, according to the data of Mössbauer spectroscopy presented in [11], with an increase in the annealing temperature above 600 °C, the magnetic ordering degree practically did not change, which indicated that the processes of structural and magnetic ordering at these temperatures reach their limit, and a subsequent increase in the annealing temperature does not lead to serious changes associated with ordering. At the same time, an increase in the annealing temperature above 600 °C led to particles sticking together with the subsequent formation of large agglomerates, which is unacceptable in the practical application of nanoparticles, in particular in biomedical applications, in which the size of objects is very important.

## 2.3. Characterization

Determination of the phase composition of the studied samples of nanoparticles, depending on the type of modification, was carried out using X-ray diffraction methods, implemented on a D8 Advance Eco powder diffractometer (Bruker, Berlin, Germany) and

MiniFlex 600 (Rigaku Corporation, Tokyo, Japan) diffractometer. The diffraction patterns were taken in the Bragg–Brentano geometry, in the angular range  $2\theta = 20\text{--}80^\circ$ , scanning speed 1 sec per point, and scanning step  $2\theta = 0.03^\circ$ ; the parameters were refined using the DiffraEVA v.4.2 software.

Morphological studies were carried out using transmission electron microscopy, implemented using a Jeol JEM-1400Plus microscope (Jeol, Tokyo, Japan).

Determination of the size of nanoparticles using the laser diffraction method was carried out using an Analysette 22 instrument (Fritsch, Germany).

Mössbauer studies applicable to the determination of hyperfine magnetic parameters of the synthesized nanoparticles were carried out at room temperature using an MS1104m Mössbauer spectrometer, where  $\text{Co}^{57}$  in an Rh matrix was used as a source. The obtained Mössbauer spectra were analyzed using the SpectrRelax software.

#### 2.4. Hyperthermia Research

Study of the modification effect of  $\text{Fe}_3\text{O}_4$  nanoparticles in various ways on the heating rate and change in the specific absorption rate was carried out using an SPG-10AB-II variable-frequency induction heater manufactured by Shuangping Power Supply Technologies Company Ltd., (Shanghai, China).

Experimental conditions: current value 20 A, alternating magnetic field with an amplitude of 210 Oe and a frequency of 320 kHz. The heating of the flask with the test solution was carried out using a copper spiral with a diameter of 6 cm, consisting of 4 turns. The magnetic field strength was calculated based on the geometry of the coil and the magnitude of the current. The flask with the test solution was placed inside the magnetic coil and isolated from the environment in order to prevent heat transfer and heat loss. The temperature control of the solution was carried out using fiber-optic thermometers placed in the liquid; these changes were read every 5 s. Aqueous solutions with 10 mg/mL nanoparticles dissolved in them were used as model solutions.

The specific absorption rate (SAR), which characterizes the heat-conducting properties of nanoparticles, was calculated according to the Equation (1):

$$SAR = \frac{M}{m_{nanoparticles}} C_{water} \frac{\Delta T}{\Delta t}, \quad (1)$$

where  $M$  is the mass of the solution,  $m_{nanoparticles}$  is the mass of nanoparticles (10 mg),  $C_{water}$  is the specific heat capacity of the solution, and  $\Delta T/\Delta t$  is the slope of the temperature curve. In view of the low concentration of nanoparticles, their heat capacity was not taken into account, and the value of the specific heat of water was chosen as  $C_{water}$ .

Intrinsic loss power (ILP), expressed as a quadratic dependence on the magnetic field and a linear dependence on frequency, as a rule, allows one to compare the heating efficiency in hyperthermic studies conducted with different samples or at different magnetic field strength parameters. The following expression was used to determine the ILP value; Equation (2):

$$ILP = SAR/H^2 f, \quad (2)$$

where  $H$  is the applied field strength,  $f$ —Frequency.

All experiments to assess the applicability of magnetic nanoparticles in hyperthermia were carried out in five successive experiments on the implementation of heating and subsequent cooling, the main purpose of which was to establish the preservation of the stability of the heating rate, as well as the stability of the conservation of heat release values. Based on the data obtained, the measurement errors were determined, and it was also found that the studied nanoparticles after five successive cycles show the invariance of the results in terms of heat release and heating rate.

### 2.5. Corrosion Resistance Tests

Tests for corrosion resistance of the selected objects of study were carried out using aqueous solutions with neutral pH = 7 at different ambient temperatures:  $T_{water} = 25\text{ }^{\circ}\text{C}$ ,  $T_{water} = 35\text{ }^{\circ}\text{C}$ ,  $T_{water} = 42\text{ }^{\circ}\text{C}$ . The degree of change in sample mass (DMC) after 10 days of corrosion was estimated using the Equation (3):

$$DMC = \frac{m_0 - m_{10}}{m_0} \times 100\% \quad (3)$$

where  $m_0$  and  $m_{10}$  are the mass values of the samples in the initial state and after being in the medium for 10 days.

These tests were carried out to determine the stability of nanoparticles in aqueous solutions at various temperatures, which can be used in the preparation, long-term storage or operation of nanoparticles. Determining the stability and understanding the time frames for maintaining the stability of the properties of nanoparticles is a very important task for further practical applications of nanoparticles. It is also necessary to know about the mechanisms or the rate of degradation of nanoparticles during their interaction with aqueous solutions, since degradation processes can lead to the destruction of the material and the loss of its magnetic characteristics or the preservation of the stability of structural parameters.

The stability of nanoparticles is determined by the amount of weight loss, as well as the crystallinity degree (degree of structural ordering), which should not exceed 10% of the initial values. At the same time, several previous studies have shown that the processes of corrosion and degradation of nanoparticles have a pronounced dependence on the phase composition of nanoparticles, as well as the structural ordering degree [11,19].

## 3. Results and Discussion

### 3.1. Results of Characterization of the Studied Nanostructures

Figure 1 shows the results of X-ray diffraction of the studied nanoparticles, reflecting the phase composition of the nanoparticles. The general view of the presented diffraction patterns indicates nanoscale structures (low intensity of reflections, as well as their broadened shape). In this case, depending on the modification, the shape of the diffraction reflections, as well as their position, changes, which indicates the occurrence of processes of phase transformations associated with the processes of substitution or insertion.

In the case of the initial samples of the synthesized particles, the position of the main observed reflections is typical for the structures of the  $\text{Fe}_3\text{O}_4$  cubic phase (PDF-01-071-6363) with the crystal lattice parameter  $a = 8.370 \pm 0.001\text{ \AA}$  and crystallite sizes of 13–15 nm (according to the estimate using the Scherrer formula, Eq.4 [20]). The characteristic phase composition of the synthesized nanoparticles by the proposed method was also established in [11].

$$D = \frac{K\lambda}{\beta \cos \theta} \quad (4)$$

where  $K$  is the Scherrer constant,  $\lambda$  is wave length of the X-ray beam used ( $1.54\text{ \AA}$ ),  $\beta$  is the full width at half maximum (FWHM) of the peak and  $\theta$  is the Bragg angle.

For samples of nanoparticles annealed at a temperature of  $600\text{ }^{\circ}\text{C}$ , a change in the shape of diffraction reflections is observed, as well as the appearance of new reflections, the general pattern of which is typical for the rhombohedral phase of hematite  $\alpha\text{-Fe}_2\text{O}_3$  with parameters  $a = 5.026 \pm 0.001\text{ \AA}$ ,  $c = 13.757 \pm 0.0021\text{ \AA}$  and crystallite sizes of 35–37 nm. Such a change in the phase composition of the  $\text{Fe}_3\text{O}_4 \rightarrow \alpha\text{-Fe}_2\text{O}_3$  type is typical for annealing temperatures of  $400\text{--}700\text{ }^{\circ}\text{C}$ , and is also accompanied not only by phase transformations, but also by an increase in the size of crystallites [11]. Estimating the shape of diffraction reflections, we can conclude that thermal annealing at a temperature of  $600\text{ }^{\circ}\text{C}$  leads not only to phase transformations of  $\text{Fe}_3\text{O}_4 \rightarrow \alpha\text{-Fe}_2\text{O}_3$ , but also to structural ordering of the

crystal structure, due to a decrease in the contribution of disordered regions and a decrease in deformation and distorting contributions [11].

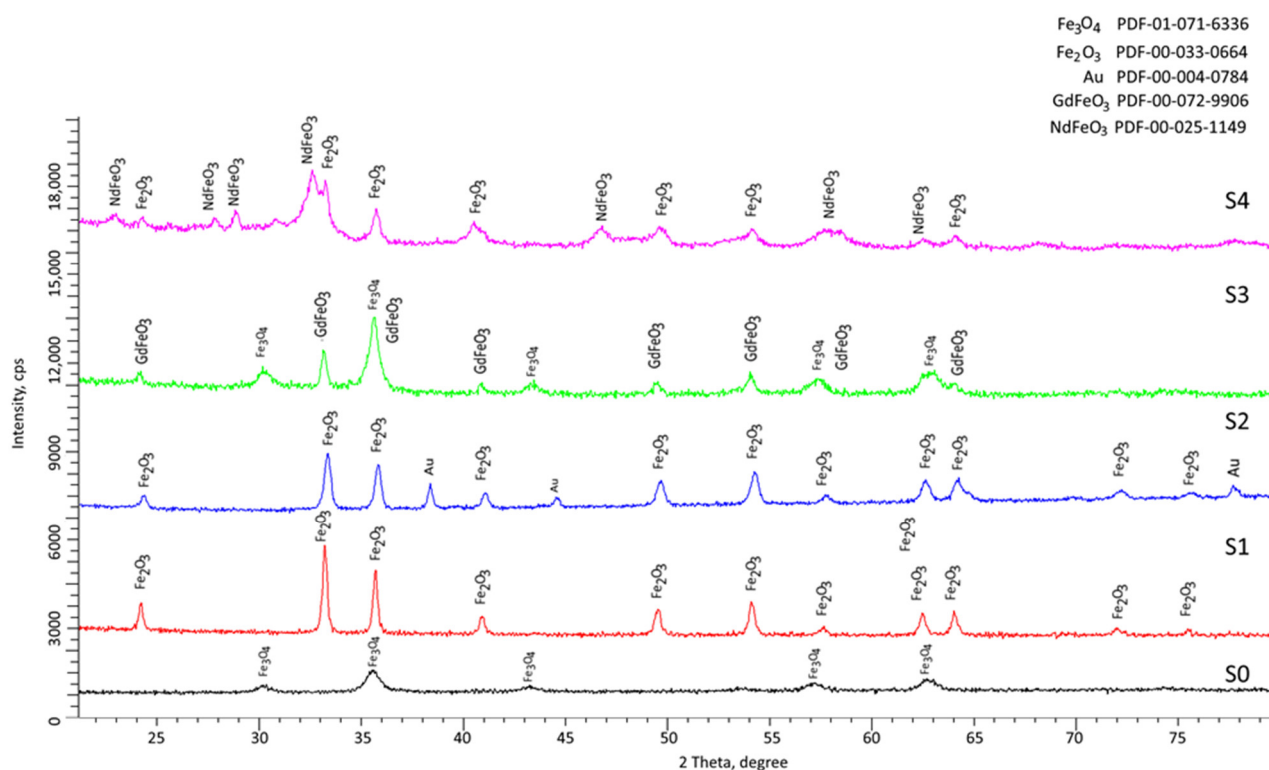


**Figure 1.** Results of X-ray diffraction of the studied nanoparticles.

In the case of samples of  $\text{Fe}_3\text{O}_4$  nanoparticles coated with gold (deposited by the method of chemical reduction of gold from its chloride solution) and then annealed at a temperature of  $600\text{ }^\circ\text{C}$ , the main phase is the  $\alpha\text{-Fe}_2\text{O}_3$  hematite phase with parameters  $a = 5.0089 \pm 0.0011\text{ \AA}$ ,  $c = 13.7219 \pm 0.0017\text{ \AA}$  and crystallite sizes of 26–27 nm. At the same time, diffraction reflections characteristic of the cubic gold phase are also observed in the diffraction pattern. The presence of two phases, according to a number of studies [21,22], is characteristic of structures of the “magnetic core–shell” type, which are obtained by forming a shell of gold on the surface of a magnetic particle, and during subsequent thermal annealing, ordering of such structures occurs.

In the case of nanoparticle samples doped with Gd by mechanochemical mixing of chemically synthesized  $\text{Fe}_3\text{O}_4$  nanoparticles with  $\text{Gd}(\text{NO}_3)_3 \times 6(\text{H}_2\text{O})$  and annealed at a temperature of  $600\text{ }^\circ\text{C}$ , the diffraction pattern shows peaks characteristic of two phases: the cubic phase of  $\text{Fe}_3\text{O}_4$  with parameters  $a = 8.325 \pm 0.0012\text{ \AA}$  and the orthorhombic phase of  $\text{GdFeO}_3$  with parameters  $a = 5.376 \pm 0.002\text{ \AA}$ ,  $b = 5.585 \pm 0.002\text{ \AA}$ ,  $c = 7.712 \pm 0.001\text{ \AA}$ . The volume ratio of  $\text{Fe}_3\text{O}_4/\text{GdFeO}_3$  phases is 70/30. The average crystallite size for both phases is no more than 27–30 nm. At the same time, the increase in the size of the crystal lattice of the  $\text{Fe}_3\text{O}_4$  phase can be explained by the partial replacement of iron ions by gadolinium ions, without the formation of a complex oxide phase of the  $\text{GdFeO}_3$  type [23].

For samples obtained by mechanochemical mixing of chemically synthesized  $\text{Fe}_3\text{O}_4$  nanoparticles with  $\text{Nd}_2\text{O}_3$  and subsequent thermal annealing at a temperature of  $600\text{ }^\circ\text{C}$ , the dominant phase in the structure is the orthorhombic phase of  $\text{NdFeO}_3$  with crystal lattice parameters  $a = 5.567 \pm 0.001\text{ \AA}$ ,  $b = 7.806 \pm 0.002\text{ \AA}$ ,  $c = 5.458 \pm 0.002\text{ \AA}$ . The structure also contains the  $\alpha\text{-Fe}_2\text{O}_3$  phase with parameters  $a = 5.027 \pm 0.002\text{ \AA}$ ,  $c = 13.762 \pm 0.002\text{ \AA}$ , the content of which is no more than 30 wt.%. The average crystallite size for these nanoparticles is no more than 30 nm.

Figure 2 presents the results of a study of nanoparticle morphology depending on the modification type. As can be seen from the data presented, in the case of the initial nanoparticles, their shape is close to spherical, and the particle sizes are comparable with the results of X-ray diffraction. In the case of nanoparticles annealed at a temperature of 600 °C, there is an increase in size, while maintaining a spherical shape. For nanoparticles of the  $\text{Fe}_2\text{O}_3@Au$  type, according to transmission microscopy data, it is clearly seen that the synthesized structures are a “core-shell”, where the core size is close to 20–23 nm, and the shell thickness is no more than 2–3 nm. For  $\text{Fe}_3\text{O}_4@GdFeO_3$  and  $\alpha\text{-Fe}_2\text{O}_3@NdFeO_3$  nanoparticles, a change in the shape of particles from spherical to ellipsoidal or rhomboid is observed, which is typical for structures with a mixed phase composition. The agglomeration of magnetic particles is due to the presence of high surface energy between the prepared magnetic nanoparticles and the presence of magnetic dipole-dipole interactions [24].

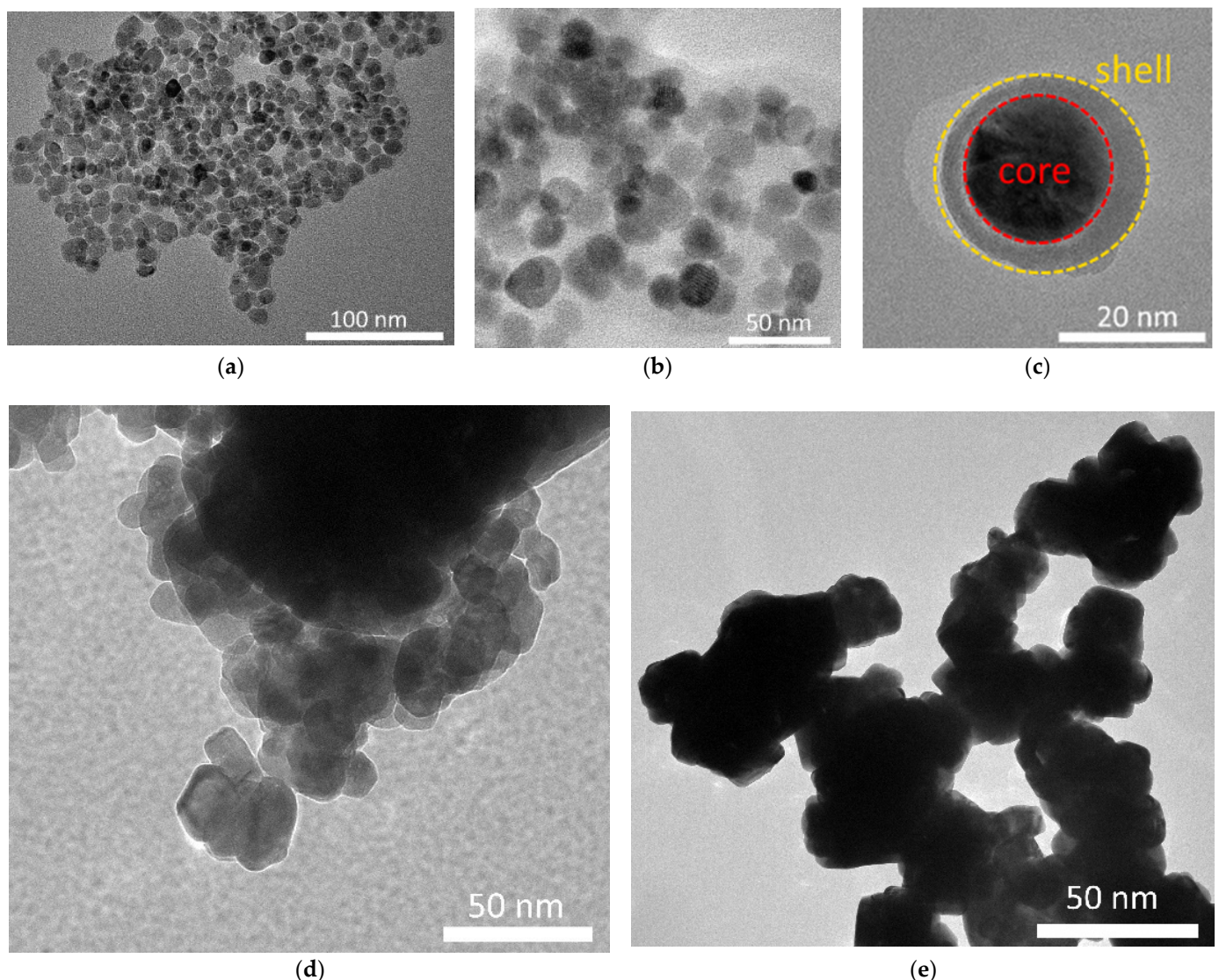


**Figure 2.** TEM images of the studied nanostructures: (a) S0; (b) S1; (c) S2; (d) S3; (e) S4.

In a detailed analysis of the obtained TEM images (see data in Figures 3 and 4) of samples S3 and S4, which, according to X-ray diffraction data, are composite two-phase structures, it was found that the synthesized S3 particles are a combination of two-phase particles. In contrast, for sample S4, it was found that the particles are structures close to the “core-shell” type, where the  $\alpha\text{-Fe}_2\text{O}_3$  particle remains as the core, and  $\text{NdFeO}_3$  as the shell. This type for S4 can be explained by the fact that the presence of a small  $\alpha\text{-Fe}_2\text{O}_3$

core surrounded by  $\text{NdFeO}_3$  is due to incomplete processes of phase transformations of the  $\alpha\text{-Fe}_2\text{O}_3 \rightarrow \text{NdFeO}_3$  type associated with partial replacement of iron ions by neodymium ions in  $\alpha\text{-Fe}_2\text{O}_3$  with subsequent rearrangement into  $\text{NdFeO}_3$ .

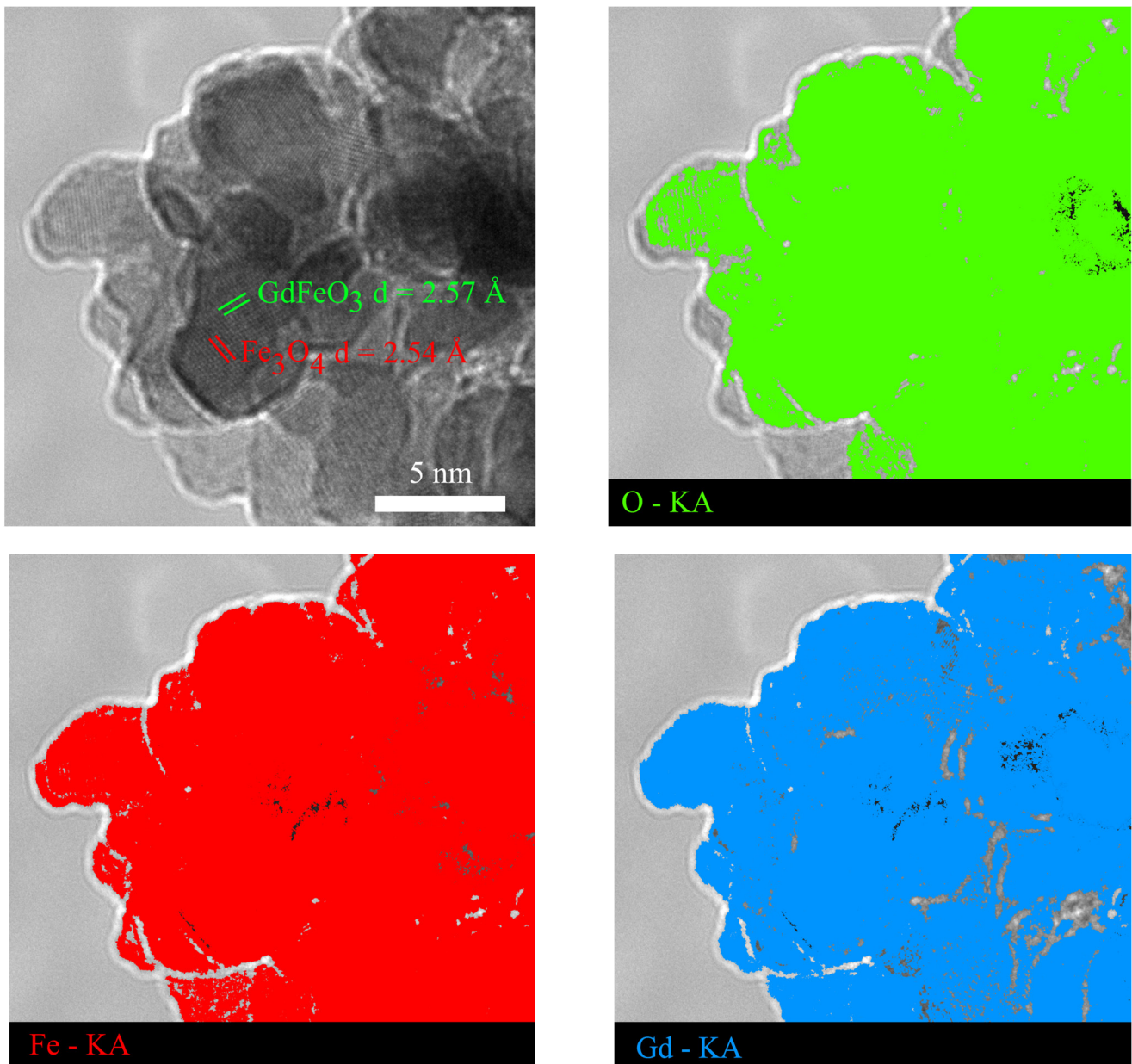


**Figure 3.** TEM data and energy dispersive analysis of the studied S3 samples.

Figure 5 presents the results of a comparative analysis of the results of measuring the sizes of nanoparticles obtained using three methods: X-ray diffraction (using the Scherrer formula), transmission electron microscopy (size estimation by direct counting using ImageJ software), laser diffraction method.

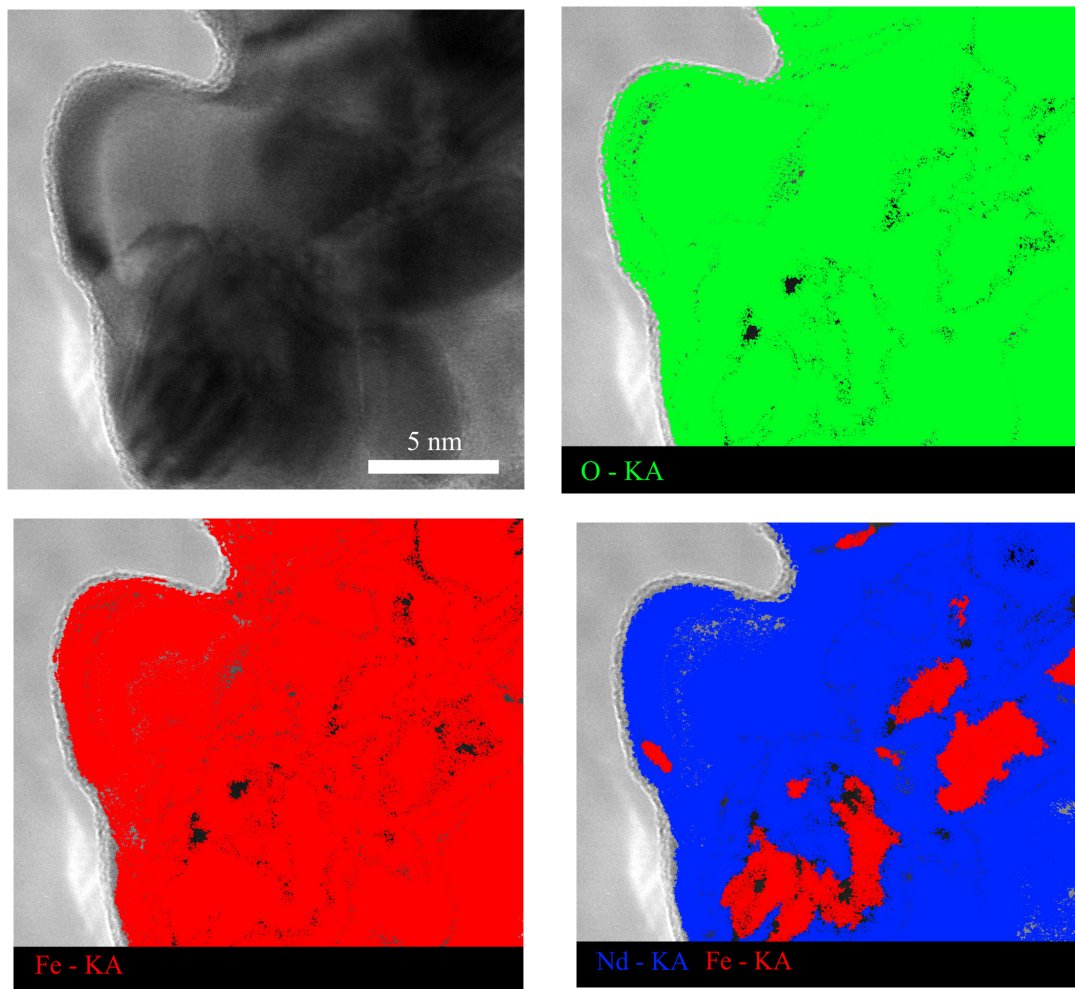


**Figure 4.** TEM data and energy dispersive analysis of the studied S4 samples.

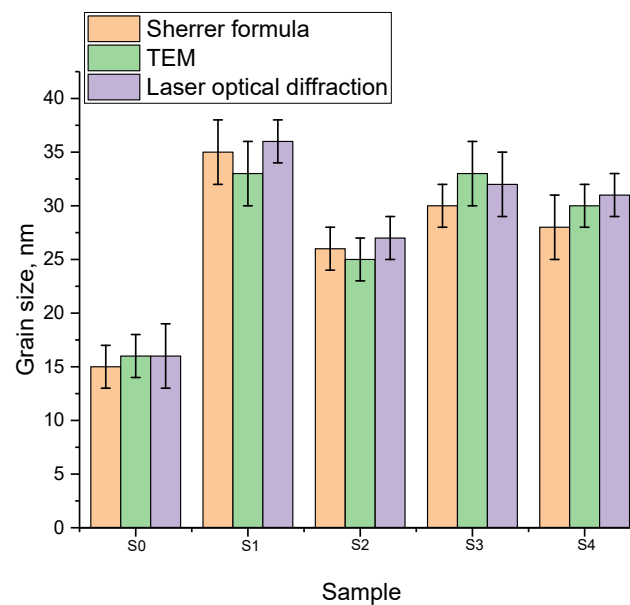


**Figure 5.** Results of comparative analysis of nanoparticle size measurements.

The general view of the presented comparative analysis data indicates a good agreement between the sizes of nanoparticles determined by various methods. A small difference

in size, which is within the error for various methods, can be explained by the peculiarities of the method of determination, as well as the geometric shape, which is most important in determining the size by electron microscopy and laser optical diffraction.

Figure 6 shows the results of a model interpretation of the Mössbauer spectra of the studied nanoparticles, reflecting their phase composition and magnetic properties. All Mössbauer spectra were taken at room temperature and contain partial spectra of iron-containing phases. Model interpretation of the spectra was carried out assuming the presence in the spectra of contributions from iron oxides with different degrees of oxidation of Fe atoms: double iron (II, III) oxide  $\text{Fe}_3\text{O}_4$  and iron (III) oxide  $\alpha\text{-Fe}_2\text{O}_3$  (for all studied nanoparticles), as well as gadolinium ferrites  $\text{GdFeO}_3$  (for  $\text{Fe}_3\text{O}_4/\text{Gd}(\text{NO}_3)_3 \cdot 6\text{H}_2\text{O}$  nanoparticles or  $\text{NdFeO}_3$  neodymium (for  $\text{Fe}_3\text{O}_4/\text{NdFeO}_3$  nanoparticles).

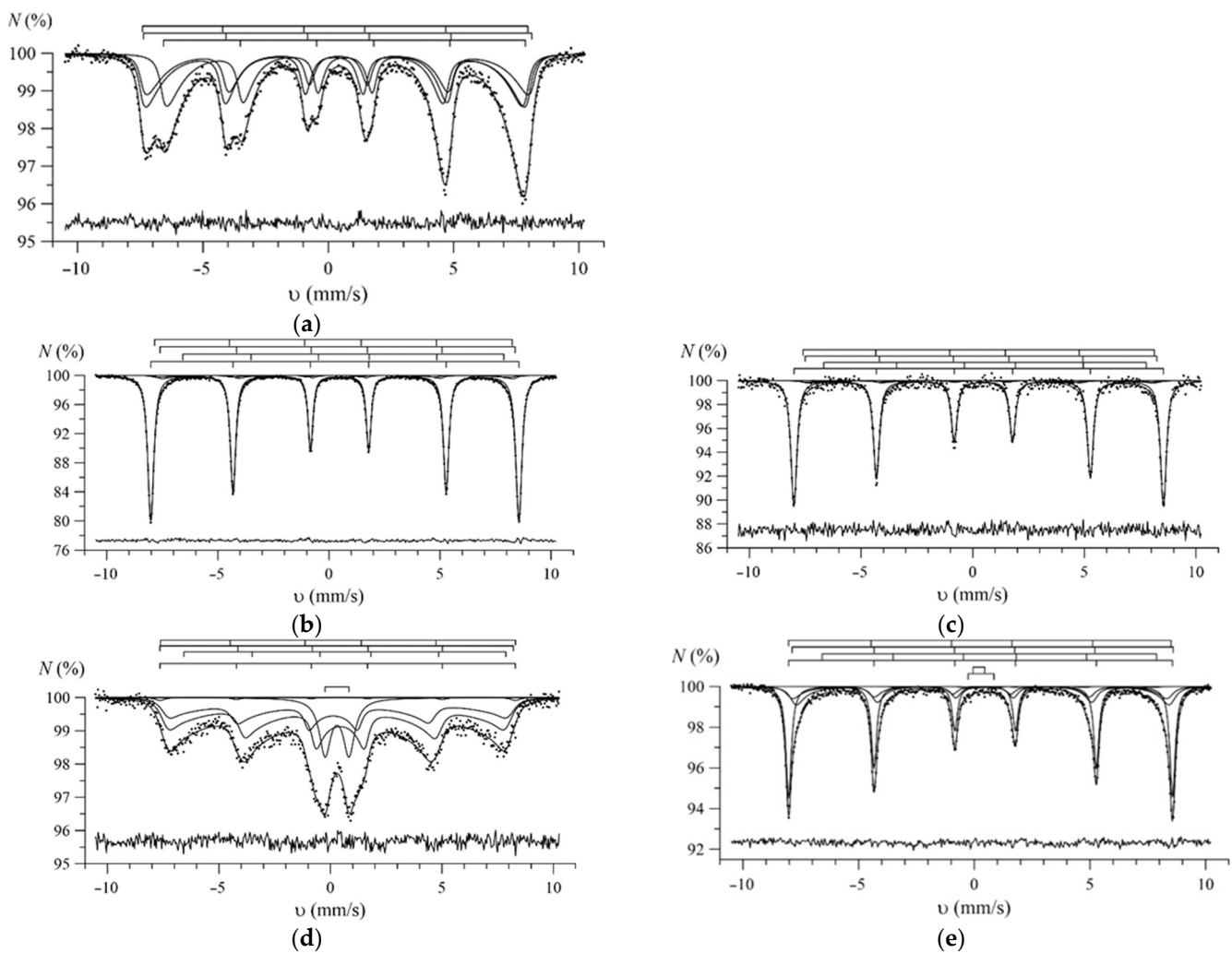


**Figure 6.** Mössbauer spectra of the studied nanoparticles: (a) S0— $\text{Fe}_3\text{O}_4$  (initial), (b) S1— $\text{Fe}_3\text{O}_4$  (600 °C), (c) S2— $\text{Fe}_3\text{O}_4/\text{Au}$  (600 °C), (d) S3— $\text{Fe}_3\text{O}_4/\text{Gd}(\text{NO}_3)_3 \cdot 6\text{H}_2\text{O}$  (600 °C), (e) S4— $\text{Fe}_3\text{O}_4/\text{NdFeO}_3$  (600 °C); above the spectra are dashed diagrams of partial spectra indicating the positions of resonance lines; below the spectra are the difference spectra.

Double iron (II, III) oxide  $\text{Fe}_3\text{O}_4$  in nanoparticles can be represented either in the form of non-stoichiometric magnetite  $\text{Fe}_{3-\gamma}\text{O}_4$ , or in the form of a combination of stoichiometric magnetite  $\text{Fe}_3\text{O}_4$  and maghemite  $\gamma\text{-Fe}_2\text{O}_3$ , which can be in the superparamagnetic state. In accordance with this, the spectrum of the double oxide was generally described by three partial relaxation spectra corresponding to Fe atoms in three different structural and valence states: trivalent  $\text{Fe}^{3+}$  ions in tetrahedral (A) and octahedral (B) positions,  $\text{Fe}_A^{3+}$  and  $\text{Fe}_B^{3+}$ , and  $\text{Fe}^{2.5+}$  ions in the octahedral position— $\text{Fe}_B^{2.5+}$ . For all the studied samples, a slow

relaxation of the magnetization of superparamagnetic particles of double iron oxide was assumed, when the relaxation rate is noticeably lower than the reciprocal lifetime of the  $^{57}\text{Fe}$  nucleus in the excited state ( $\tau = 1.4 \times 10^{-7}$  s). A detailed description of the model of the spectrum of double iron oxide nanoparticles, which takes into account both the rapid exchange of electrons between neighboring atoms in pairs  $\{\text{Fe}_B^{2+}\text{Fe}_B^{3+}\}$  in the octahedral position of the magnetite structure, and the possible superparamagnetic relaxation, is presented in our previously published works [25–27]. This model makes it possible to determine the values of the following spectrum parameters and physical quantities for double iron oxide (Table 1):

**Table 1.** Model interpretation results of the Mössbauer spectra of the studied nanoparticles.

Sample	Atom State	<i>I</i> , %	$\delta$ , mm/s	$\epsilon$ , mm/s	$H_{in}$ , kOe	$\alpha$	$\gamma$	<i>b</i>	$K_{eff}$ , $10^6 \text{J} \cdot \text{m}^{-3}$	<i>d</i> , Å					
S0	Fe <sub>3</sub> O <sub>4</sub> (initial)	Fe <sub>A</sub> <sup>3+</sup>	36.7 ± 0.2	0.26 ± 0.02	0.02 ± 0.02	476.8 ± 1.0	6.39 ± 0.12	0.165 ± 0.005	0.49 ± 0.02	11.4 ± 0.8	16.4 ± 0.4				
		Fe <sub>B</sub> <sup>3+</sup>	28.4 ± 0.1	0.39 ± 0.02	−0.02 ± 0.03	480.6 ± 1.4									
		Fe <sub>B</sub> <sup>2.5+</sup>	34.9 ± 0.2	0.66 ± 0.01	−0.01 ± 0.01	447.9 ± 0.7									
S1	Fe <sub>3</sub> O <sub>4</sub> (600 °C)	Fe <sub>A</sub> <sup>3+</sup>	3.0 ± 0.2	0.19-fix	0.01-fix	499-fix	7.75-fix	0.314 ± 0.003	0.94 ± 0.01	5.0 ± 0.9	23.0 ± 1.5				
		Fe <sub>B</sub> <sup>3+</sup>	4.7 ± 0.2	0.43-fix	−0.04-fix	495-fix									
		Fe <sub>B</sub> <sup>2.5+</sup>	0.00 ± 0.01	0.66-fix	−0.01-fix	448-fix									
		α-Fe <sub>2</sub> O <sub>3</sub>	92.3 ± 0.2	0.372 ± 0.002	−0.108 ± 0.002	513.9 ± 0.2						-	-	-	-
S2	Fe <sub>2</sub> O <sub>3</sub> @Au (600 °C)	Fe <sub>A</sub> <sup>3+</sup>	3.1 ± 0.6	0.24-fix	0.03-fix	488-fix	6.90-fix	0.332 ± 0.009	1.00 ± 0.26	5.0 ± 0.8	22.1 ± 1.2				
		Fe <sub>B</sub> <sup>3+</sup>	4.9 ± 0.2	0.37-fix	0.00-fix	489-fix									
		Fe <sub>B</sub> <sup>2.5+</sup>	0.00 ± 0.01	0.66-fix	−0.01-fix	448-fix									
		α-Fe <sub>2</sub> O <sub>3</sub>	92.0 ± 0.6	0.372 ± 0.002	−0.106 ± 0.002	513.3 ± 0.2						-	-	-	-
S3	Fe <sub>3</sub> O <sub>4</sub> / Gd(NO <sub>3</sub> ) <sub>3</sub> ·6H <sub>2</sub> O (600 °C)	Fe <sub>A</sub> <sup>3+</sup>	32.7 ± 1.3	0.28 ± 0.04	0.16 ± 0.04	486.9 ± 2.9	2.08 ± 0.12	0.333 ± 0.012	1.00 ± 0.05	5.0 ± 0.6	14.8 ± 0.6				
		Fe <sub>B</sub> <sup>3+</sup>	51.3 ± 0.7	0.36 ± 0.07	−0.08 ± 0.07	482.7 ± 4.0									
		Fe <sub>B</sub> <sup>2.5+</sup>	0.00 ± 0.02	0.66-fix	−0.01-fix	448-fix									
		GdFeO <sub>3</sub>	1.4 ± 1.8	0.36-fix	−0.04-fix	494-fix						-	-	-	-
		doublet	14.6 ± 0.8	0.29 ± 0.02	0.55 ± 0.02	-						-	-	-	-
S4	Fe <sub>2</sub> O <sub>3</sub> /Nd <sub>2</sub> O <sub>3</sub> (600 °C)	Fe <sub>A</sub> <sup>3+</sup>	6.8 ± 0.4	0.28-fix	0.06 ± 0.03	487-fix	3.61 ± 0.22	0.333 ± 0.025	1.00 ± 0.08	5.0 ± 0.9	17.8 ± 1.0				
		Fe <sub>B</sub> <sup>3+</sup>	10.6 ± 0.1	0.36-fix	−0.10 ± 0.02	483-fix									
		Fe <sub>B</sub> <sup>2.5+</sup>	0.00 ± 0.01	0.66-fix	−0.01-fix	448-fix									
		α-Fe <sub>2</sub> O <sub>3</sub>	58.7 ± 1.9	0.373 ± 0.002	−0.097 ± 0.002	515.1 ± 0.2						-	-	-	-
		NdFeO <sub>3</sub>	24.0 ± 2.2	0.361 ± 0.005	−0.052 ± 0.005	499.5 ± 0.8						-	-	-	-

$\alpha$ —multilevel superparamagnetic relaxation model parameter equal to the ratio of the magnetic anisotropy energy  $K_{\text{eff}}V$  to the thermal energy  $k_{\text{B}}T$ ;

$\gamma$ —the number of vacancies in the octahedral position of Fe ( $0 \leq \gamma \leq 1/3$ ) atoms per  $\text{Fe}_{3-\gamma}\text{O}_4$  formula unit (degree of nonstoichiometry of magnetite  $\text{Fe}_{3-\gamma}\text{O}_4$ );

$b = 3\gamma$ —molar concentration of maghemite ( $0 \leq b \leq 1$ ) in a mixture of stoichiometric magnetite  $\text{Fe}_3\text{O}_4$  and maghemite  $\gamma\text{-Fe}_2\text{O}_3$ ;

$K_{\text{eff}}$ —magnetic anisotropy coefficient at room temperature;

$d$ —the size of the magnetic ordering region.

The data obtained as a result of model interpretation of the Mössbauer spectra of the studied nanoparticles (Figure 6) are presented in Table 1. In accordance with the data obtained, sample S0 is a set of nanoparticles, the composition of which can be represented either as  $\text{Fe}_{3-\gamma}\text{O}_4$  with a degree of nonstoichiometry  $\gamma = 0.165 \pm 0.005$ , or a mixture of stoichiometric phases of magnetite and maghemite with a molar concentration of maghemite  $b = 0.49 \pm 0.2$ . The found values of the hyperfine parameters of the partial spectra, constituting the shift of the Mössbauer spectrum  $\delta$ , the quadrupole shift  $\varepsilon$  of the spectrum components, and the hyperfine magnetic field  $H_{\text{n}}$  in the region where the  $^{57}\text{Fe}$  nucleus is located, are in good agreement with the structural and valence states of Fe atoms in nonstoichiometric magnetite [28]. The average size of the regions of magnetic ordering of magnetite nanoparticles is  $16.4 \pm 0.4$  nm, which is in good agreement with the values obtained by XRD and TEM (Figure 3).

Upon annealing of the initial nanoparticles at a temperature of 600 °C (sample S1), a significant modification of the Mössbauer spectrum occurs (Figure 6b), a phase transformation of iron (II, III) double oxide into hematite  $\alpha\text{-Fe}_2\text{O}_3$  (92.3%) is observed, while the remaining part of the oxide (7.7%) is mainly nanoparticles of maghemite  $\gamma\text{-Fe}_2\text{O}_3$  ( $b = 0.94 \pm 0.01$ ,  $\gamma = 0.314 \pm 0.003$ ) with an average size of magnetic ordering regions  $d = 23.0 \pm 1.5$  nm (Table 1). The obtained values of the hyperfine parameters of  $\alpha\text{-Fe}_2\text{O}_3$  hematite correspond to the literature data [29]. Note that when a small amount of double iron oxide  $\text{Fe}_3\text{O}_4$  was determined in the Mössbauer spectra of the studied nanoparticles, we used the values of the hyperfine parameters of its partial spectra obtained at a lower temperature of thermal annealing of the nanoparticles, when it was possible to reliably determine the values of the hyperfine parameters of  $\text{Fe}_3\text{O}_4$  (Table 1).

The shape of the Mössbauer spectrum of gold-coated  $\text{Fe}_3\text{O}_4$  nanoparticles (sample S2) (Figure 6c) is almost the same as the spectrum of uncoated nanoparticles (S1). The values of the hyperfine parameters of these two spectra turn out to be close (see Table 1). Annealing of gold-coated  $\text{Fe}_3\text{O}_4$  nanoparticles also leads to the phase transformation of iron (II, III) double oxide into hematite  $\alpha\text{-Fe}_2\text{O}_3$  (92.0%), and its remaining part (7.3%) to complete transformation into maghemite  $\gamma\text{-Fe}_2\text{O}_3$  ( $b = 1.00 \pm 0.26$ ,  $\gamma = 0.332 \pm 0.009$ ) with the average size of the regions of magnetic ordering being  $d = 22.1 \pm 1.2$  nm.

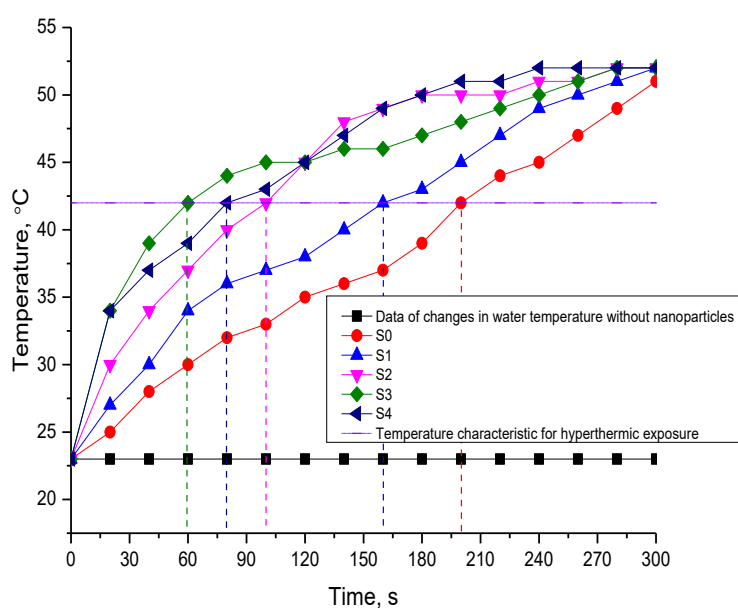
Figure 6d shows the Mössbauer spectrum of the annealed  $\text{Fe}_3\text{O}_4/\text{Gd}(\text{NO}_3)_3 \cdot 6\text{H}_2\text{O}$  nanoparticles (sample S3), which has a pronounced relaxation nature and for which a paramagnetic contribution from the quadrupole doublet is observed in the central region of the spectrum. This spectrum was interpreted by three partial relaxation spectra corresponding to double iron oxide  $\text{Fe}_3\text{O}_4$ , a Zeeman sextet with hyperfine parameters characteristic of  $\text{GdFeO}_3$  ferrite [30–32], and a quadrupole doublet. As a result, it turned out that the nanoparticles of the composite consist mainly of maghemite  $\gamma\text{-Fe}_2\text{O}_3$  (~84%) with an average size of magnetic ordering regions  $d = 14.8 \pm 0.6$  nm, presumably of iron- and gadolinium-containing nanoregions in the paramagnetic or superparamagnetic state (~15%), and a small amount of  $\text{GdFeO}_3$  (~1%) (Table 1).

Figure 6e shows the Mössbauer spectrum of the annealed  $\text{Fe}_3\text{O}_4/\text{NdFeO}_3$  nanoparticles (sample S4). This spectrum was interpreted by three partial spectra corresponding to double iron oxide  $\text{Fe}_3\text{O}_4$  and two Zeeman sextets. The hyperfine parameters of one of them correspond to hematite  $\alpha\text{-Fe}_2\text{O}_3$  [29], and the other to  $\text{NdFeO}_3$  ferrite [33–35] (Table 1). Double iron oxide is maghemite  $\gamma\text{-Fe}_2\text{O}_3$  ( $b = 1.00 \pm 0.08$ ,  $\gamma = 0.333 \pm 0.025$ ) with an average size of magnetic ordering regions of  $d = 17.8 \pm 1.0$  nm. In this case, the relative

contributions to the spectrum of nanoparticles from the partial spectra of hematite  $\alpha\text{-Fe}_2\text{O}_3$ , ferrite  $\text{NdFeO}_3$ , and maghemite  $\gamma\text{-Fe}_2\text{O}_3$  are  $\sim 59\%$ ,  $\sim 24\%$  and  $\sim 17\%$ , respectively.

### 3.2. Results of Hyperthermic Studies

Results of the temperature measurements of aqueous solutions with nanoparticles placed in them (10 mg/mL) depending on the time of induction heating are shown in Figure 7. The obtained dependences characterize the heating rate of nanoparticles, as well as the maximum heating temperature that the solutions reach in 300 s. For comparison, the results of hyperthermic studies of an aqueous solution without nanoparticles are presented in order to determine the effect of a magnetic field on water heating. Results of a comparative experiment showed the absence of any effect of an alternating magnetic field on the heating of an aqueous solution during the experiment, from which it can be concluded that the solution with nanoparticles placed in it is heated only due to heat transfer from magnetic particles.



**Figure 7.** Results of determining the temperature dependences of heating.

As can be seen from the presented  $T(t)$  dependences, in the case of the initial  $\text{Fe}_3\text{O}_4$  nanoparticles, the threshold heating temperature of  $42\text{ }^\circ\text{C}$  (the horizontal dashed line in the Figure 7, reflecting the value of  $42\text{ }^\circ\text{C}$ , the characteristic temperature for hyperthermia) is reached in 200 s, which is quite low and indicates a small amount of heat release. In the case of  $\text{Fe}_3\text{O}_4$  nanoparticles annealed at a temperature of  $600\text{ }^\circ\text{C}$ , which are characterized by a highly ordered hematite phase, the heating time is  $\sim 160$  s, which is somewhat better than the analogous parameters for the initial  $\text{Fe}_3\text{O}_4$  nanoparticles. Such a decrease in the heating time to a temperature of  $42\text{ }^\circ\text{C}$  may be due to a change in the phase composition of the nanoparticles, which leads to a change in the values of the hyperfine magnetic field.

In the case of nanoparticles, the heating time compared to the initial nanoparticles changes significantly. For  $\text{Fe}_3\text{O}_4\text{@Au}$  NPs, the heating time was 100 s; for  $\text{Fe}_3\text{O}_4\text{@GdFeO}_3$  NPs, 60 s; and for  $\text{Fe}_2\text{O}_3\text{@NdFeO}_3$  NPs, 80 s.

Based on the dependences obtained  $T(t)$ , the heating rate of the aqueous solution was calculated for all types of the studied nanoparticles. The heating rate was calculated for all the samples under study by determining the time required to reach the threshold temperature of  $42\text{ }^\circ\text{C}$ , typical for hyperthermic effects. Importantly, for human exposure, it is pivotal to maintain the product of the magnetic field strength (H) and its frequency (f) below a threshold safety value known as the Brezovich criterion. A safety limit commonly prescribed is that the product of the frequency and the field amplitude ( $C = H \times f$ ) should

remain below  $5 \times 10^9$  A/(ms) to minimize any collateral effects of alternating magnetic fields on the human body [36,37]. The choice of this temperature is due to the need to initialize the mechanisms of inhibition of the recovery of tumor cells damaged by radiation or drug therapy. The calculation results are shown in Figure 8.

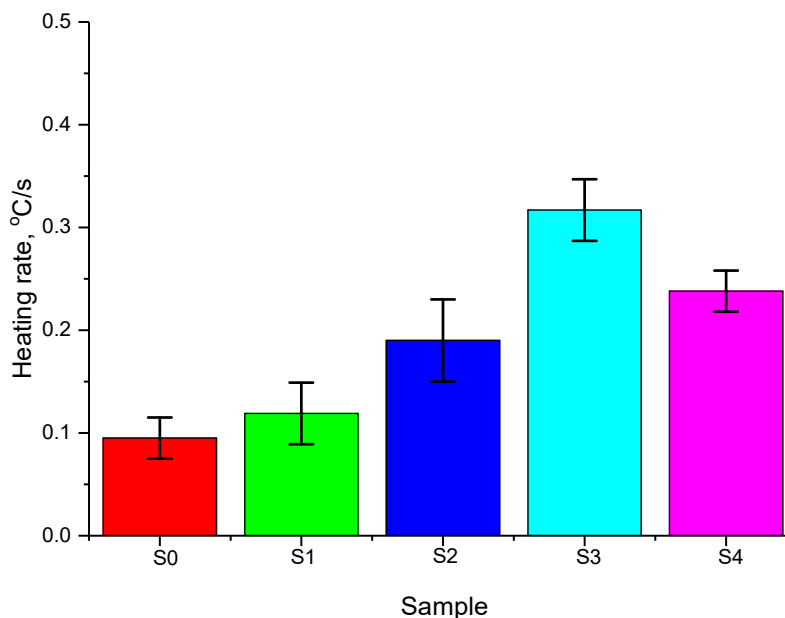


**Figure 8.** Diagram of the change in the heating rate of nanoparticles depending on their type.

According to the data obtained, the modification of nanoparticles leads to an increase in the heating rate, as well as a decrease in the time required to reach the threshold value. At the same time,  $\text{Fe}_3\text{O}_4@\text{GdFeO}_3$  nanoparticles have the maximum heating rate, for which the heating rate is three times higher than that for the initial nanoparticles.

An increase in the heating efficiency for nanoparticles is due to a change in the magnetic characteristics, as well as an increase in the rate of energy absorption and release of additional heat. The exchange coupling effect between the hard and soft phases in the core-shell structure may improve some magnetic properties, such as coercivity ( $H_c$ ) and saturation magnetization ( $M_s$ ), possibly resulting in the enhancement of heat-generation performance of the magnetic NPs [36,37]. In the case of using  $\text{Fe}_3\text{O}_4@\text{GdFeO}_3$  nanoparticles, which are characterized by the presence of two phases in the structure of  $\text{Fe}_3\text{O}_4$  and  $\text{GdFeO}_3$ , the substitution of gadolinium ions for iron ions in the crystal lattice leads to the highest energy absorption.

Results of change in the specific absorption rate are presented in Figure 9a. The calculations were carried out using the aforementioned expression (Equation (1)).

According to the data obtained, a change in the phase composition of nanoparticles from  $\text{Fe}_3\text{O}_4$  to  $\text{Fe}_2\text{O}_3$  as a result of thermal annealing at a temperature of  $600^\circ\text{C}$  leads to an increase in the specific absorption rate by 25%, while the modification of nanoparticles with various components leads to an increase in the specific absorption rate by 1.2–2 times depending on the modification type. Similar dependencies are obtained for the ILP value, the results of which are shown in Figure 9b.

### 3.3. Results of a Comparative Analysis of Magnetic Hyperthermia with Literature Data

One of the important characteristics of magnetic nanoparticles in the case of their use in magnetic hyperthermia is the value of the SAR parameter, which makes it possible to estimate the efficiency of energy absorption and subsequent heat release for various types of nanoparticles. In most cases of magnetic nanoparticles, the SAR value is 60–80 W/g, and also has a clear dependence on the applied field frequency. At the same time, as shown

in [38], the concentration of nanoparticles plays an ambiguous role when changing the field frequency in the case of determining the SAR value. Figure 10 presents the results of a small comparative analysis of the effectiveness of the SAR value of the studied nanoparticles with the literature data from [38–41].

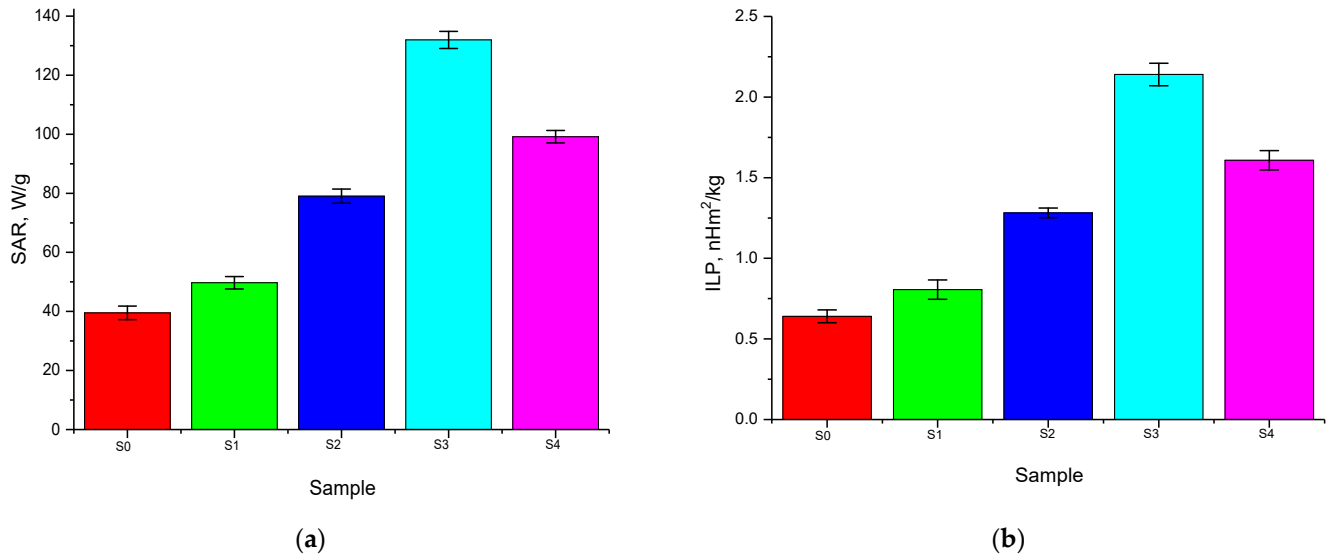


Figure 9. SAR (a) and ILP (b) diagrams for all studied nanoparticles.

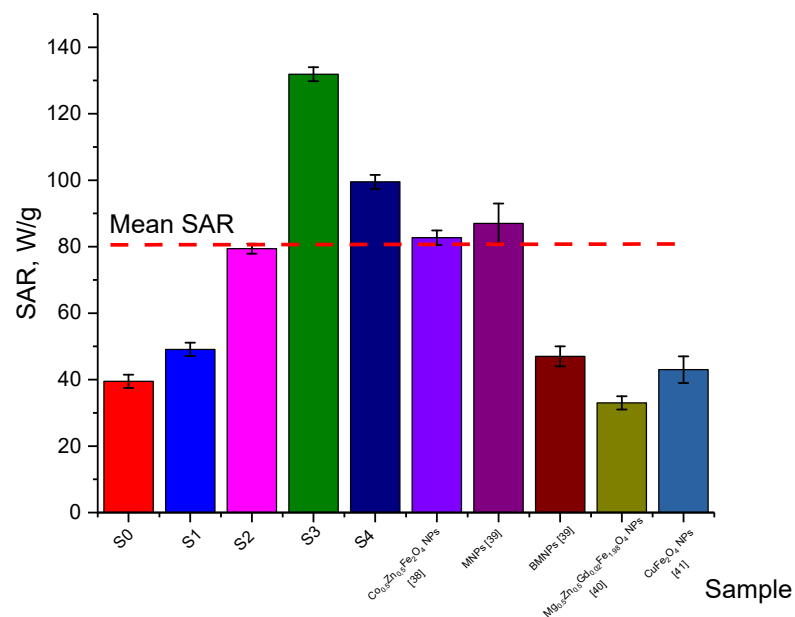


Figure 10. Results of a comparative analysis of the SAR value efficiency.

As can be seen from the data presented, the most effective (not only in comparison with the results of this work, but also in comparison with the literature data) are the structures of Fe<sub>3</sub>O<sub>4</sub>@GdFeO<sub>3</sub> NPs and Fe<sub>2</sub>O<sub>3</sub>@NdFeO<sub>3</sub> NPs, for which the SAR value exceeds other types of nanoparticles by 1.5–2 times.

Table 2 presents the results of a comparative analysis of the conditions of action on magnetic nanoparticles (magnetic field strength and frequency), as well as these *ILP* values, which in most cases are a universal value for determining the efficiency of heat transfer, since this value includes not only the values of the heating rate, but also the conditions of external influences by a magnetic field.

**Table 2.** Comparison of the obtained *SAR* and *ILP* data with the literature data, taking into account the conditions of exposure to the magnetic field.

Sample	Amplitude of the Magnetic Field	The Frequency, kHz	<i>SAR</i> , W/g	<i>ILP</i> , nHm <sup>2</sup> /kg	Ref.
S0	210 Oe	320	39 ± 2	0.6 ± 0.1	Present work
S1			49 ± 2	0.8 ± 0.2	
S2			79 ± 2	1.3 ± 0.1	
S3			132 ± 5	2.1 ± 0.3	
S4			99 ± 3	1.6 ± 0.2	
Co <sub>0.5</sub> Zn <sub>0.5</sub> Fe <sub>2</sub> O <sub>4</sub> NPs	167.5–335.2 Oe	197–280	83 ± 2	0.9–1.1	[38]
MNPs	167–335 Oe	265	87 ± 3	0.96–1.04	[39]
BMNPs			47 ± 4	0.50–0.52	[39]
Mg <sub>0.5</sub> Zn <sub>0.5</sub> Gd <sub>0.02</sub> Fe <sub>1.98</sub> O <sub>4</sub> NPs	5 kA/m	600	33 ± 3	0.2–0.3	[40]
CuFe <sub>2</sub> O <sub>4</sub> NPs	13–19 kA/m	120	43 ± 2	1.04–1.23	[41]

As can be seen from the data presented, despite the fact that the efficiency of the *SAR* value can reach different values, the heat transfer efficiency depends quite strongly on the amplitude of the external field, as well as the applied frequency, which is quite clearly manifested in the change in the *ILP* value. At the same time, according to comparative data on *ILP* and *SAR* values, nanoparticles of the Fe<sub>3</sub>O<sub>4</sub>@GdFeO<sub>3</sub> NPs and Fe<sub>2</sub>O<sub>3</sub>@NdFeO<sub>3</sub> NPs types can be considered the most effective not only in comparison with the results of this study, but also with literature data.

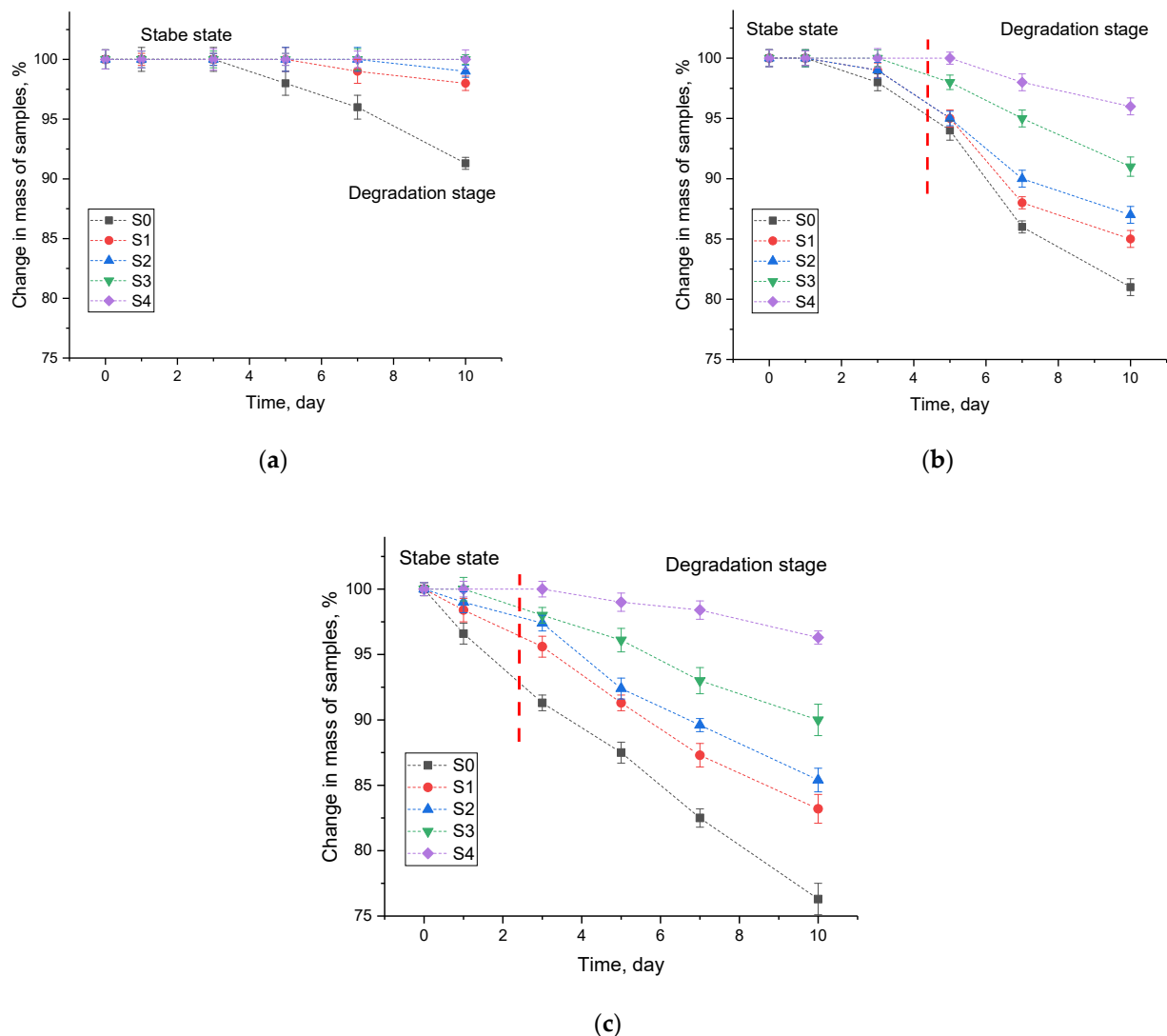
### 3.4. Results of Nanoparticle Corrosion Test

Figure 11 shows the results of the temporal change in the mass of samples in aqueous media at different temperatures, reflecting the corrosion processes. The choice of test temperatures is due to the possibilities of their operation, as well as different variations in the temperature of the medium at which they can be in the case of transportation or use. The assessment of the corrosion resistance of the studied nanoparticles was carried out by measuring the mass defect of the samples during testing at different time intervals. The measurements were carried out by weighing the samples after certain time intervals on an analytical balance; to collect statistics, all experiments were carried out in five parallels.

The general trends in the change in the mass of samples over time can be divided into two characteristic stages, which have different time intervals with a change in the temperature of the solution, as well as types of modification of nanoparticles.

The first stage is characterized by the stage of stability, as a result of which changes in the mass of the samples are either not observed or are so small that they are within the measurement error. This stage indicates the stability of the synthesized nanoparticles when they are in aqueous solutions, as well as the absence or slow processes of corrosion and oxidation.

The second stage is characteristic of a decrease in the mass of samples, which indicates the processes of degradation of nanoparticles, as well as their partial or complete destruction, leading to a decrease in the total mass of the particles under study. At the same time, a decrease in the mass of samples indicates that when nanoparticles are in an aqueous solution, the main corrosion mechanisms are associated with the processes of oxygen and hydrogen incorporation into the surface layer of nanoparticles, with the formation of oxides or hydroxide inclusions, followed by decomposition of nanoparticles, and their decomposition into components. At the same time, these processes have a pronounced dependence on the temperature of the aqueous solution.



**Figure 11.** Changes in the masses of the samples as a result of corrosion tests at different temperatures of the aqueous solution: (a)  $T_{water} = 25\text{ }^{\circ}\text{C}$ ; (b)  $T_{water} = 35\text{ }^{\circ}\text{C}$ ; (c)  $T_{water} = 42\text{ }^{\circ}\text{C}$ .

In the case of a solution temperature of  $T_{water} = 25\text{ }^{\circ}\text{C}$ , the most pronounced degradation processes associated with a change in mass were observed for samples of  $\text{Fe}_3\text{O}_4$  NPs, for which the maximum change in mass after 10 days of being in an aqueous solution was 7–8%. For samples of nanoparticles annealed at a temperature of  $600\text{ }^{\circ}\text{C}$   $\text{Fe}_3\text{O}_4$  NPs and  $\text{Fe}_2\text{O}_3@Au$  NPs, the most noticeable mass changes were observed only after 5 days of being in an aqueous solution, and after 10 days, the mass change was no more than 1–2%, which also indicates a fairly high degradation resistance. The decrease in the mass of samples indicates that when nanoparticles are in aqueous solution, the main corrosion mechanisms are associated with the processes of oxidation and subsequent decomposition of nanoparticles, and their decay into components. For samples of  $\text{Fe}_3\text{O}_4@GdFeO_3$  NPs and  $\text{Fe}_2\text{O}_3@NdFeO_3$  NPs, no change in mass was observed after 10 days of being in an aqueous solution at a temperature of  $25\text{ }^{\circ}\text{C}$ , which indicates a sufficiently high resistance of nanoparticles to degradation processes as a result of corrosion (see the results of Figure 12).

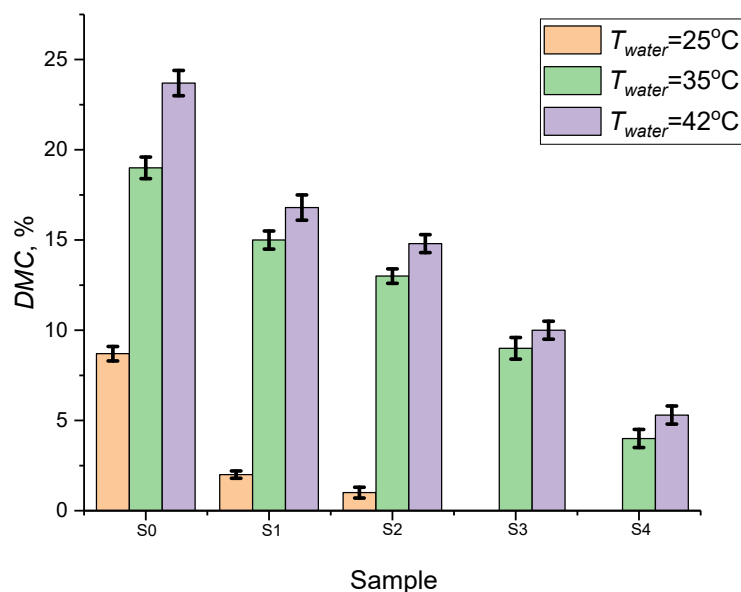


**Figure 12.** Results of sample masses change after 10 days in aqueous medium.

For the solution temperature of  $T_{water} = 35^{\circ}\text{C}$ , degradation processes are more pronounced, which is reflected in an increase in mass loss not only for  $\text{Fe}_3\text{O}_4$  NPs, but also for all other types of nanoparticles. At the same time, analyzing the obtained dependences of the mass change on time, it can be concluded that the corrosion rate increases significantly at a temperature of  $T_{water} = 35^{\circ}\text{C}$ , as evidenced by the fact that mass changes begin to be observed after 3–4 days of testing. At the same time,  $\text{Fe}_3\text{O}_4@ \text{NdFeO}_3$  NPs proved to be the most effective in terms of corrosion resistance, for which the value of weight loss after 10 days in the environment was less than 5%, which is practically four times less than the similar value for  $\text{Fe}_3\text{O}_4$  NPs. Such a significant difference in the corrosion rate and mass loss for the studied samples with increasing solution temperature can be explained by the presence of two phases in the  $\text{Fe}_3\text{O}_4@ \text{NdFeO}_3$  NPs structure, which reduce the corrosion propagation rate due to the presence of interfacial boundaries. In the case of  $\text{Fe}_2\text{O}_3@ \text{Au}$  NPs, the decrease in the corrosion rate can be explained by the presence of a gold shell, which is less active in corrosion processes, leading to a decrease in the degradation rate.

For solution temperatures  $T_{water} = 42^{\circ}\text{C}$ , an increase in the corrosion rate is observed, and as a result, an increase in mass loss occurs, which reflects the degradation of the structure of nanoparticles. This behavior at elevated solution temperatures can be explained by the fact that an increase in temperature leads to an increase in the mobility of ions in water, thereby accelerating the process of their interaction with the surface of nanoparticles, leading to the appearance of local corrosion centers, which increase with time, leading to degradation of nanoparticles due to their small sizes.

Figure 13 shows the data on changes in the degree of structural disorder (degree of degradation) for the studied nanoparticles after 10 days of being in aqueous solutions at different ambient temperatures, reflecting the resistance of the synthesized nanoparticles to structural degradation. The data of X-ray diffraction analysis of the studied samples after corrosion tests were used for calculations.

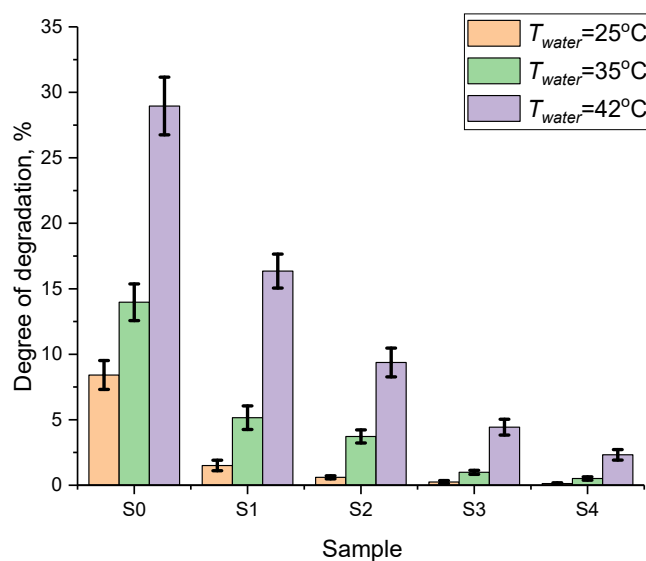


**Figure 13.** Data on the change in the degradation degree of the studied nanoparticles depending on the temperature of the medium.

According to the data obtained, the change in the degradation degree has a good agreement with the data on changes in the mass loss of the samples as a result of corrosion, which indicates that the processes of structural degradation are directly related to the weight loss of the samples, the decrease of which may be due to the effects of partial destruction of the surface of nanoparticles due to the processes of oxidation and subsequent decomposition, which leads to a decrease in the mass of the particle, and the dissolved precipitate remains in the form of oxide or hydroxide compounds of a finely dispersed fraction in an aqueous solution, being in a paramagnetic state or a fine suspension that is not affected by a magnetic field during capture and filtration.

As can be seen from the data presented, the most pronounced structural degradation is observed for samples that were in an aqueous medium at a temperature of 42 °C, for which corrosion processes, as it was established from the data on the change in the mass of samples, begin to actively manifest themselves after 1–3 days, and the maximum change in the mass of the samples in the case of the original unmodified nanoparticles is more than 20%. Similar dependences of structural degradation are also observed when assessing the structural ordering degree, according to which, for unmodified samples after 10 days of exposure to aqueous media, a serious change in the values of structural ordering is observed, and the obtained diffraction patterns revealed the presence of low-intensity reflections characteristic of hydroxide inclusions, which indicates the processes of destruction associated with the formation of new impurity inclusions in nanoparticles or their passivation.

For annealed  $\text{Fe}_3\text{O}_4$  nanoparticles at a temperature of 600 °C, for which, according to the data of X-ray phase analysis, the  $\text{Fe}_3\text{O}_4 \rightarrow \text{Fe}_2\text{O}_3$  phase transformation is observed and an increase in the degree of structural ordering due to partial relaxation of deformation distortions that have arisen during synthesis, an almost two to threefold decrease in the degradation degree is observed in comparison with the initial  $\text{Fe}_3\text{O}_4$  nanoparticles. This difference indicates that the main mechanisms of nanoparticle destruction during corrosion tests are deformation during oxidation, as well as the presence of deformation distortions in the structure, a high concentration of which leads to accelerated degradation of nanoparticles, which was observed in the case of  $\text{Fe}_3\text{O}_4$  nanoparticles.

At the same time, for modified nanoparticles, the degree of structural degradation is significantly less after 10 days of corrosion testing, which, as a result, indicates a high resistance of nanoparticles to degradation and corrosion degradation. In the case of  $\text{Fe}_3\text{O}_4@\text{Au}$

nanoparticles, the degree of degradation at a temperature of 25 °C is less than 1.5% after 10 days of exposure to the medium, which indicates that the presence of a gold shell leads to a significant decrease in the rate of degradation and structural disorder. However, an increase in the corrosion test temperature leads to an increase in the degree of structural disorder, the value of which is at least 10% for the test temperature  $T_{water} = 42$  °C.

For  $Fe_3O_4@GdFeO_3$  and  $Fe_2O_3@NdFeO_3$  nanoparticles, structural disordering after 10 days of corrosion testing at  $T_{water} = 25$  °C was not established, and the observed changes are within the error, which indicates a high resistance of these nanostructures to corrosion processes. At the same time,  $Fe_2O_3@NdFeO_3$  nanoparticles are more resistant to degradation and structural disorder at  $T_{water} = 42$  °C, for which the maximum decrease in the crystallinity degree was no more than 3–4%, which indicates a high resistance to destruction of these nanoparticles.

Analyzing the general dependences of the presented data of corrosion tests, it can be concluded that  $Fe_3O_4@NdFeO_3$  NPs and  $Fe_3O_4@GdFeO_3$  NPs are the most resistant to degradation processes in aqueous solutions, for which the degradation resistance can be explained by the presence of interfacial boundaries, leading to a decrease in the corrosion propagation rate.

#### 4. Conclusions

During the studies, it was found that thermal annealing of iron-containing nanoparticles at a temperature of 600 °C leads to the initialization of phase transformations of the  $Fe_3O_4 \rightarrow Fe_2O_3$  type, accompanied by an increase in the degree of structural ordering and coarsening of grain sizes, due to sintering processes. At the same time, the formation of structures of the “core-shell” type during thermal annealing does not lead to coarsening of grain sizes, which indicates that during thermal annealing, the main changes associated with phase transformations and transformations occur without coarsening of grains due to their sintering, which is prevented by the presence of a gold shell. In the case of composite two-phase nanostructures, the presence of interphase boundaries leads to the formation of additional structural distortions and a slight decrease in the structural ordering degree.

Based on the obtained temperature dependences, the heating rate of the aqueous solution was calculated for all types of the studied nanoparticles. The heating rate was calculated for all samples under study by determining the time required to reach the threshold temperature of 42 °C, typical for hyperthermic studies. According to the analysis of the applicability of the synthesized nanoparticles with various types of modification, it was found that  $Fe_3O_4@GdFeO_3$  NPs, for which the heating rate is three times higher than the same value for the initial nanoparticles, have the highest efficiency.

Results of the change in the mass of samples in aqueous media over time at different temperatures, reflecting the corrosion processes, are obtained. The choice of test temperatures is due to the possibilities of their operation, as well as various variations in the temperature of the medium at which they can be in the case of transportation or use. It was found that the modification of iron-containing nanoparticles with gadolinium and neodymium with the formation of composite structures of the  $Fe_3O_4@NdFeO_3$  and  $Fe_3O_4@GdFeO_3$  type leads to an increase in the degradation resistance by a factor of 2.5–3 compared to  $Fe_3O_4$  nanoparticles. The increase in stability is due to the effects of the presence of two phases, as well as the formation of additional interphase boundaries, which reduce the degradation rate.

**Author Contributions:** Conceptualization, A.N., A.L.K., V.S.R., K.B.E., M.S.F., B.A.P., D.C., M.V.Z. and K.K.K.; methodology A.N., A.L.K., V.S.R., K.B.E., M.S.F., B.A.P., D.C., M.V.Z. and K.K.K.; formal analysis, V.S.R., A.L.K., M.S.F., K.B.E., A.N., K.K.K. and M.V.Z.; investigation, K.K.K., A.L.K., V.S.R., M.S.F., K.B.E. and A.N.; resources, K.K.K. and A.L.K.; writing—original draft preparation, review and editing, V.S.R., M.S.F. and A.L.K.; visualization, K.K.K., A.L.K., V.S.R. and M.S.F.; supervision, K.K.K. All authors have read and agreed to the published version of the manuscript.

**Funding:** This study was funded by the Ministry of Education and Science of the Republic of Kazakhstan (grant AP09259184). The authors V.S.R. and M.S.F. thank M.V. Lomonosov Moscow State University for updating the equipment for scientific research used in the work.

**Conflicts of Interest:** The authors declare no conflict of interest.

## References

1. Jose, J.; Kumar, R.; Harilal, S.; Mathew, G.E.; Parambi, D.G.T.; Prabhu, A.; Mathew, B. Magnetic nanoparticles for hyperthermia in cancer treatment: An emerging tool. *Environ. Sci. Pollut. Res.* **2020**, *27*, 19214–19225. [[CrossRef](#)] [[PubMed](#)]
2. Fatima, H.; Charinpanitkul, T.; Kim, K.-S. Fundamentals to Apply Magnetic Nanoparticles for Hyperthermia Therapy. *Nanomaterials* **2021**, *11*, 1203. [[CrossRef](#)] [[PubMed](#)]
3. Grüttner, C.; Müller, K.; Teller, J.; Westphal, F. Synthesis and functionalisation of magnetic nanoparticles for hyperthermia applications. *Int. J. Hyperth.* **2013**, *29*, 777–789. [[CrossRef](#)] [[PubMed](#)]
4. Huang, H.S.; James, F.H. Intravenous magnetic nanoparticle cancer hyperthermia. *Int. J. Nanomed.* **2013**, *8*, 2521.
5. Ramana, P.V.; Rao, K.S.; Kumar, K.R.; Kapusetti, G.; Choppadandi, M.; Kiran, J.N.; Rao, K.H. A study of uncoated and coated nickel-zinc ferrite nanoparticles for magnetic hyperthermia. *Mater. Chem. Phys.* **2021**, *266*, 124546. [[CrossRef](#)]
6. Ramirez, D.; Oliva, J.; Cordova-Fraga, T.; Basurto-Islas, G.; Benal-Alvarado, J.J.; Mtz-Enriquez, A.I.; Quintana, M.; Gomez-Solis, C. High Heating Efficiency of Magnetite Nanoparticles Synthesized with Citric Acid: Application for Hyperthermia Treatment. *J. Electron. Mater.* **2022**, *51*, 4425–4436. [[CrossRef](#)]
7. Islam, M.S.; Kusumoto, Y.; Kurawaki, J.; Abdulla-Al-Mamun, M.D.; Manaka, H. A comparative study on heat dissipation, morphological and magnetic properties of hyperthermia suitable nanoparticles prepared by co-precipitation and hydrothermal methods. *Bull. Mater. Sci.* **2012**, *35*, 1047–1053. [[CrossRef](#)]
8. Dey, C.; Baishya, K.; Ghosh, A.; Goswami, M.M.; Ghosh, A.; Mandal, K. Improvement of drug delivery by hyperthermia treatment using magnetic cubic cobalt ferrite nanoparticles. *J. Magn. Magn. Mater.* **2017**, *427*, 168–174. [[CrossRef](#)]
9. Macías-Martínez, B.I.; Cortés-Hernández, D.A.; Zugasti-Cruz, A.; Cruz-Ortiz, B.R.; Múzquiz-Ramos, E.M. Heating ability and hemolysis test of magnetite nanoparticles obtained by a simple co-precipitation method. *J. Appl. Res. Technol.* **2016**, *14*, 239–244. [[CrossRef](#)]
10. Jang, D.-H.; Lee, Y.-I.; Kim, K.-S.; Park, E.-S.; Kang, S.-C.; Yoon, T.-J.; Choa, Y.-H. Induced heat property of polyethyleneglycol-coated iron oxide nanoparticles with dispersion stability for hyperthermia. *J. Nanosci. Nanotechnol.* **2013**, *13*, 6098–6102. [[CrossRef](#)]
11. Kozlovskiy, A.L.; Ermekova, A.E.; Korolkov, I.V.; Chudoba, D.; Jazdzewska, M.; Ludzik, K.; Zdorovets, M.V. Study of phase transformations, structural, corrosion properties and cytotoxicity of magnetite-based nanoparticles. *Vacuum* **2019**, *163*, 236–247. [[CrossRef](#)]
12. McBain, S.C.; Yiu, H.H.P.; Dobson, J. Magnetic nanoparticles for gene and drug delivery. *Int. J. Nanomed.* **2008**, *3*, 169–180.
13. Xu, S.H.; Fei, G.T.; Ouyang, H.M.; Zhang, Y.; Huo, P.C.; De Zhang, L. Controllable fabrication of nickel nanoparticle chains based on electrochemical corrosion. *J. Mater. Chem. C* **2014**, *3*, 2072–2079. [[CrossRef](#)]
14. Durgadsimi, S.U.; Kattimani, V.R.; Maruti, N.S.; Kulkarni, A.B.; Mathad, S.N. Synthesis and structural analysis of nickel ferrite synthesized by co-precipitation method. *Eurasian Phys. Tech. J.* **2021**, *18*, 14–19. [[CrossRef](#)]
15. Fayazzadeh, S.; Khodaei, M.; Arani, M.; Mahdavi, S.R.; Nizamov, T.; Majouga, A. Magnetic Properties and Magnetic Hyperthermia of Cobalt Ferrite Nanoparticles Synthesized by Hydrothermal Method. *J. Supercond. Nov. Magn.* **2020**, *33*, 2227–2233. [[CrossRef](#)]
16. Ebrahimisadr, S.; Aslibeiki, B.; Asadi, R. Magnetic hyperthermia properties of iron oxide nanoparticles: The effect of concentration. *Phys. C Supercond. Its Appl.* **2018**, *549*, 119–121. [[CrossRef](#)]
17. Hasany, S.F.; Ahmed, I.; Rajan, J.; Rehman, A. Systematic Review of the Preparation Techniques of Iron Oxide Magnetic Nanoparticles. *Nanosci. Nanotechnol.* **2012**, *2*, 148–158. [[CrossRef](#)]
18. He, S.; Feng, Y.; Ren, H.; Zhang, Y.; Gu, N.; Lin, X. The impact of iron oxide magnetic nanoparticles on the soil bacterial community. *J. Soils Sediments* **2011**, *11*, 1408–1417. [[CrossRef](#)]
19. Stary, O.; Malyshev, A.V.; Lysenko, E.N.; Petrova, A. Formation of magnetic properties of ferrites during radiation-thermal sintering. *Eurasian Phys. Tech. J.* **2021**, *17*, 6–10. [[CrossRef](#)]
20. Smilgies, D.-M. Scherrer grain-size analysis adapted to grazing-incidence scattering with area detectors. *J. Appl. Crystallogr.* **2009**, *42*, 1030–1034. [[CrossRef](#)]
21. León Félix, L.; Coaquira, J.A.H.; Martínez, M.A.R.; Goya, G.F.; Mantilla, J.; Sousa, M.H.; Morais, P.C. Structural and magnetic properties of core-shell Au/Fe<sub>3</sub>O<sub>4</sub> nanoparticles. *Sci. Rep.* **2017**, *7*, 41732. [[CrossRef](#)] [[PubMed](#)]
22. Ghorbani, M.; Hamishehkar, H.; Arsalani, N.; Entezami, A.A. Preparation of thermo and pH-responsive polymer@ Au/Fe<sub>3</sub>O<sub>4</sub> core/shell nanoparticles as a carrier for delivery of anticancer agent. *J. Nanoparticle Res.* **2015**, *17*, 305. [[CrossRef](#)]
23. Zhang, Y.; Zheng, A.; Yang, X.; He, H.; Fan, Y.; Yao, C. Cubic GdFeO<sub>3</sub> particle by a simple hydrothermal synthesis route and its photoluminescence and magnetic properties. *Crystengcomm* **2012**, *14*, 8432–8439. [[CrossRef](#)]
24. Darwish, M.S.A.; Stibor, I. Pentenoic Acid-Stabilized Magnetic Nanoparticles for Nanomedicine Applications. *J. Dispers. Sci. Technol.* **2016**, *37*, 1793–1798. [[CrossRef](#)]

25. Fadeev, M.; Kozlovskiy, A.; Korolkov, I.; Egizbek, K.; Nazarova, A.; Chudoba, D.; Rusakov, V.; Zdorovets, M. Iron oxide @ gold nanoparticles: Synthesis, properties and potential use as anode materials for lithium-ion batteries. *Colloids Surfaces A: Physicochem. Eng. Asp.* **2020**, *603*, 125178. [[CrossRef](#)]
26. Korolkov, I.; Ludzik, K.; Kozlovskiy, A.; Fadeev, M.; Shumskaya, A.; Gorin, Y.; Marciniak, B.; Jazdzewska, M.; Chudoba, D.; Kontek, R.; et al. Carboranes immobilization on Fe<sub>3</sub>O<sub>4</sub> nanocomposites for targeted delivery. *Mater. Today Commun.* **2020**, *24*, 101247. [[CrossRef](#)]
27. Korolkov, I.; Ludzik, K.; Kozlovskiy, A.; Fadeev, M.; Shumskaya, A.; Gorin, Y.; Jazdzewska, M.; Anisovich, M.; Rusakov, V.; Zdorovets, M. Immobilization of carboranes on Fe<sub>3</sub>O<sub>4</sub>-polymer nanocomposites for potential application in boron neutron cancer therapy. *Colloids Surfaces A Physicochem. Eng. Asp.* **2020**, *601*, 125035. [[CrossRef](#)]
28. Mashlan, M.; Zboril, R.; Machala, L.; Vujtek, M.; Walla, J.; Nomura, K. Mössbauer spectroscopy in study of thermally induced crystallization of amorphous Fe<sub>2</sub>O<sub>3</sub> nanoparticles. *J. Metastable Nanocryst. Mater.* **2004**, *20–21*, 641–647.
29. Ristić, M.; De Grave, E.; Musić, S.; Popović, S.; Orehovec, Z. Transformation of low crystalline ferrihydrite to  $\alpha$ -Fe<sub>2</sub>O<sub>3</sub> in the solid state. *J. Mol. Struct.* **2006**, *834–836*, 454–460. [[CrossRef](#)]
30. Paesano, A.; Zanatta, S.C.; De Medeiros, S.N.; Cótica, L.F.; Da Cunha, J.B.M. Mechanosynthesis of YIG and GdIG: A Structural and Mössbauer Study. *Hyperfine Interact.* **2005**, *161*, 211–220. [[CrossRef](#)]
31. Silva, C.L.S.; Marchetti, S.G.; Faro, A.C.; Silva, T.F.; Assaf, J.M.; Rangel, M.C. Effect of gadolinium on the catalytic properties of iron oxides for WGS. *Catal. Today* **2013**, *213*, 127–134. [[CrossRef](#)]
32. Kasenov, B.K.; Kasenova, S.B.; Sagintaeva, Z.I.; Nukhuly, A.; Turtubaeva, M.O.; Bekturganov, Z.S.; Issabaeva, M.A. Synthesis and X-ray investigation of novel nanostructured copper-zinc manganites of lanthanum and alkali metals. *Eurasian Phys. Tech. J.* **2021**, *18*, 29–33. [[CrossRef](#)] [[PubMed](#)]
33. Musić, S.; Popović, S.; Ristic, M.; Sepiol, B. Chemical and structural properties of the system Fe<sub>2</sub>O<sub>3</sub>-Nd<sub>2</sub>O<sub>3</sub>. *J. Mater. Sci.* **1994**, *29*, 1714–1718. [[CrossRef](#)]
34. Lazurova, J.; Mihalik, M.; Mihalik, M.; Vavra, M.; Zentkova, M.; Briancin, J.; Perovic, M.; Kusigerski, V.; Schneeweiss, O.; Roupцова, P.; et al. Magnetic Properties and Mössbauer spectroscopy of NdFe<sub>1-x</sub>Mn<sub>x</sub>O<sub>3</sub>. *J. Phys. Conf. Ser.* **2015**, *592*, 012117. [[CrossRef](#)]
35. Scrimshire, A.; Lobera, A.; Bell, A.M.T.; Jones, A.H.; Sterianou, I.; Forder, S.D.; Bingham, P.A. Determination of Debye temperatures and Lamb–Mössbauer factors for LnFeO<sub>3</sub> orthoferrite perovskites (Ln = La, Nd, Sm, Eu, Gd). *J. Phys. Condens. Matter* **2018**, *30*, 105704. [[CrossRef](#)]
36. Darwish, M.S.A.; Kim, H.; Lee, H.; Ryu, C.; Young Lee, J.; Yoon, J. Engineering Core-Shell Structures of Magnetic Ferrite Nanoparticles for High Hyperthermia Performance. *Nanomaterials* **2020**, *10*, 991. [[CrossRef](#)]
37. Darwish, M.S.; Kim, H.; Lee, H.; Ryu, C.; Lee, J.Y.; Yoon, J. Synthesis of Magnetic Ferrite Nanoparticles with High Hyperthermia Performance via a Controlled Co-Precipitation Method. *Nanomaterials* **2019**, *9*, 1176. [[CrossRef](#)]
38. Nikam, D.; Jadhav, S.V.; Khot, V.; Phadatare, M.; Pawar, S. Study of AC magnetic heating characteristics of Co<sub>0.5</sub>Zn<sub>0.5</sub>Fe<sub>2</sub>O<sub>4</sub> nanoparticles for magnetic hyperthermia therapy. *J. Magn. Magn. Mater.* **2013**, *349*, 208–213. [[CrossRef](#)]
39. Iglesias, G.R.; Jabalera, Y.; Peigneux, A.; Fernández, B.L.C.; Delgado, Á.V.; Jimenez-Lopez, C. Enhancement of Magnetic Hyperthermia by Mixing Synthetic Inorganic and Biomimetic Magnetic Nanoparticles. *Pharmaceutics* **2019**, *11*, 273. [[CrossRef](#)]
40. Hirosawa, F.; Iwasaki, T.; Watano, S. Synthesis and magnetic induction heating properties of Gd-substituted Mg–Zn ferrite nanoparticles. *Appl. Nanosci.* **2017**, *7*, 209–214. [[CrossRef](#)]
41. Fotukian, S.M.; Barati, A.; Soleymani, M.; Alizadeh, A.M. Solvothermal synthesis of CuFe<sub>2</sub>O<sub>4</sub> and Fe<sub>3</sub>O<sub>4</sub> nanoparticles with high heating efficiency for magnetic hyperthermia application. *J. Alloys Compd.* **2020**, *816*, 152548. [[CrossRef](#)]